

Sparsity/Undersampling Tradeoffs in Anisotropic Undersampling, with Applications in MR Imaging/Spectroscopy

Hatef Monajemi*, David L. Donoho*

March 10, 2017

Abstract

We study *anisotropic* undersampling schemes like those used in multi-dimensional NMR spectroscopy and MR imaging, which sample exhaustively in certain time dimensions and randomly in others.

Our analysis shows that anisotropic undersampling schemes are equivalent to certain block-diagonal measurement systems. We develop novel exact formulas for the sparsity/undersampling tradeoffs in such measurement systems. Our formulas predict finite- N phase transition behavior differing substantially from the well known asymptotic phase transitions for classical Gaussian undersampling. Extensive empirical work shows that our formulas accurately describe observed finite- N behavior, while the usual formulas based on universality are substantially inaccurate.

We also vary the anisotropy, keeping the total number of samples fixed, and for each variation we determine the precise sparsity/undersampling tradeoff (phase transition). We show that, other things being equal, the ability to recover a sparse object decreases with an increasing number of exhaustively-sampled dimensions.

keywords: Sparse Recovery, Compressed Sensing, Block Diagonal Measurement Matrix.¹

1 Introduction

1.1 Background

In Compressed Sensing (CS), one wishes to reconstruct an N -dimensional discrete signal x_0 using $n < N$ measurements. Theory shows that if x_0 is sufficiently sparse, and the $n \times N$ sensing matrix A is an *i.i.d* Gaussian random matrix, then x_0 can be reconstructed accurately and reliably from measurements $y = Ax_0$ using convex optimization; see many papers and books, such as [6, 4, 7, 29, 15, 25, 45, 3].

In general, at a given fixed level of undersampling, the chance of successful recovery depends on the sparsity of the underlying object, in an almost binary fashion. Namely, suppose that the object x_0 is k -sparse—has at most k nonzero entries—and consider the situation where $k \sim \epsilon N$ and $n \sim \delta N$. Then, as a function of undersampling fraction $\delta = n/N$, there is a definite range of sparsity values $\epsilon = k/N$ that permits successful recovery, and outside this range, recovery is unsuccessful.

Figure 1 depicts the situation for Gaussian measurement matrices A . It shows a so-called phase diagram $(\epsilon, \delta) \in (0, 1)^2$ and a curve $\epsilon^*(\delta)$ separating a ‘success’ phase from a ‘failure’ phase. Namely, if $\epsilon < \epsilon^*(\delta)$, then with overwhelming probability for large N , convex optimization will recover x_0 exactly; while on the other hand, if $\epsilon > \epsilon^*(\delta)$, then with overwhelming probability convex optimization will fail.

Theoretical expressions for the boundary $\epsilon^*(\delta)$ separating success from failure were derived in [5, 10] assuming the measurement matrix is Gaussian and the problem size N is large. In [11, 13] they were found experimentally to describe accurately many random measurement schemes. Thorough mathematical analysis now fully supports all these findings across very large classes of random matrices [2, 38].

The same boundary $\epsilon^*(\delta)$ even applies to an important class of non-random measurement matrices, see [37], so the ‘universality’ of the compressed sensing phase transition is quite broad.

*Department of Statistics, Stanford University, Stanford, CA

¹It is a pleasure to acknowledge discussions with the pioneers of anisotropic undersampling: Jeffrey Hoch and Adam Schuyler (U. Conn. Health Sciences), Michael Lustig (UC Berkeley), John Pauly (Stanford). This research was partially supported by NSF-DMS 1418362 and NSF-DMS 1407813. We would also like to thank the Stanford Research Computing Center for providing computational resources and support that have contributed to these research results.

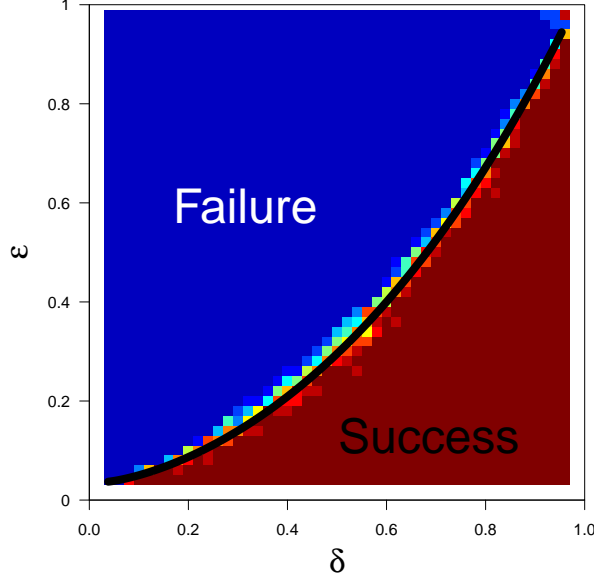


Figure 1: Success and failure regions for ‘classical’ compressed sensing with Gaussian measurement matrices; assumes object to recover is sparse and nonnegative. The asymptotic phase transition curve $\epsilon^*(\delta)$ (solid black line) separates the two regions. Shaded attribute gives fraction of successful reconstructions. Red, 100%; blue, 0%. In this experiment, $n = 250$.

As an important example, consider random Fourier undersampling in 2-dimensional Fourier imaging. The underlying object is a two-dimensional array $x_0 = (x_0(t_0, t_1), 0 \leq t_i < M)$. The traditional experiment, without undersampling, collects a two-dimensional array $(\hat{x}_0(k_0, k_1), 0 \leq k_i < M)$ of complete measurements, each one based on evaluation of the 2D Fourier transform at a specific 2D frequency index (k_0, k_1) . To implement undersampling, sample n distinct pairs $(k_{0,i}, k_{1,i})$ uniformly at random from among all such pairs. The resulting measurements vector $y = (\hat{x}_0(k_{0,i}, k_{1,i}), i = 1, \dots, n)$. Assuming the object x_0 is sparse, one attempts to reconstruct by ℓ_1 minimization:

$$(P_1^{iso}) \quad \arg \min_x \|x\|_1 \quad \text{subject to} \quad y_i = \hat{x}(k_{0,i}, k_{1,i}), \quad i = 1, \dots, n.$$

Depending on the actual sparsity level in x_0 , this strategy might be successful or unsuccessful. The phase transition from success to failure that holds for this sampling scheme has been shown [12, 37] to agree asymptotically with the phase transition curve for Gaussian measurements. Once again we underline the purported ‘universality’ of Figure 1.

However, clearly not every measurement scheme can behave equivalently to Gaussian undersampling.

1.2 Anisotropic Undersampling

This paper studies an important class of anisotropic undersampling schemes that exhibit novel theoretical behavior and arise naturally in MR imaging and NMR spectroscopy.

Let’s give a concrete example of anisotropic undersampling. As earlier, the underlying object is a 2D array $x_0 = (x_0(t_0, t_1), 0 \leq t_i < M)$. There is a 2D array $(\hat{x}_0(k_0, k_1) : 0 \leq k_i < M)$ of potential Fourier measurements. We undersample anisotropically by randomly selecting a fraction δ of the columns of the array, and then sampling everything from each selected column, producing $n = m \cdot M$ samples overall, where $m = \lfloor \delta M \rfloor$. We implement this concretely by sampling uniformly at random m distinct integers $k_{1,i}$ from the set $0 \leq k_1 < M$, yielding the partial measurements $y^{aniso} = (\hat{x}_0(k_0, k_{1,i}), i = 1, \dots, m, 0 \leq k_0 < M)$. No other samples are collected. Just as we call this sampling scheme *anisotropic*, let’s call the earlier Fourier undersampling scheme *isotropic*. The terminology reminds us that for isotropic sampling, k_0 and k_1 are scattered randomly with no directional preference, while for anisotropic sampling, the sampling scheme is exhaustive in the k_0 coordinate and random in k_1 .

Again assuming sparsity of the object to be recovered, we can attempt to reconstruct using ℓ_1 minimization:

$$(P_1^{aniso}) \quad \arg \min_x \|x\|_1 \quad \text{subject to} \quad y_{i,k_0} = \hat{x}_0(k_0, k_{1,i}), \quad i = 1, \dots, m, \quad 0 \leq k_0 < M.$$

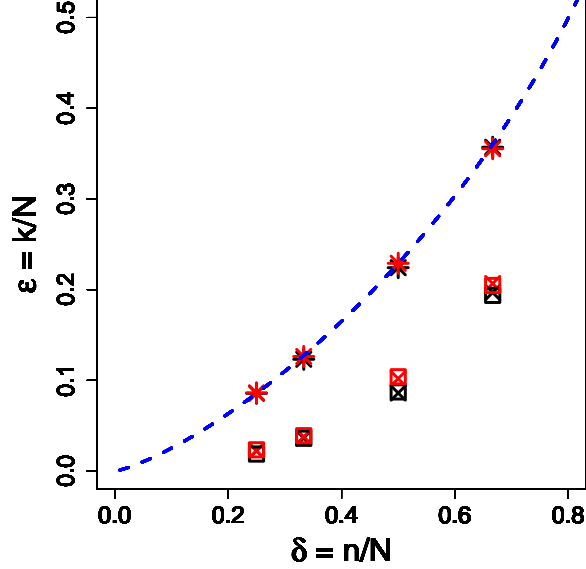


Figure 2: Equivalence of anisotropic undersampling scheme in MR imaging with block diagonal measurements studied in this paper. The \times symbol indicates anisotropic undersampling experiments using partial 2D FT where a specific fraction δ of rows are selected uniformly at random, and then each selected row is sampled exhaustively. The $*$ symbol indicates isotropic undersampling experiments using a partial 2D FT where a certain fraction of pixels are selected uniformly at random. The \square symbol indicates experimental data from a block diagonal measurement matrix with a single repeated Gaussian random matrix block. The colors indicate different problem sizes. Black stands for a 24×24 grid and red for a 48×48 grid. The dashed blue line gives the expected phase transition location for complex-valued Gaussian measurement ensembles. The isotropic undersampling data lie close to the dashed blue line, while the anisotropic undersampling data are substantially displaced.

Once again, the sparsity level determines success or failure. Figure 2 displays the empirical phase transition from success to failure for our reconstruction from anisotropic undersampling, as a function of underlying sparsity; when the object is more sparse than the depicted transition point, success is the predicted outcome, whereas when the object is less sparse than indicated, we predict failure.

Figure 2 also shows the transition known to hold for the isotropic scheme. The striking comparison is that, while there are definite phase transitions in each case, the anisotropic ones don't occur at the same place as the isotropic ones; instead the transitions for the anisotropic sampling are shifted downwards substantially from the phase transitions for the isotropic scheme. Formulas for the precise amount of shift are presented below.²

The just-described 'anisotropic' phase transitions differ noticeably from the corresponding 'isotropic' phase transitions, which are the same as the 'universal' ones known for Gaussian random matrices.

1.3 Block Diagonal Undersampling

Figure 2 displays results for three seemingly very different situations. The first two are isotropic and anisotropic undersampling in 2D Fourier imaging, respectively.

The third situation is seemingly unrelated to 2D Fourier imaging: *block-diagonal Gaussian undersampling*. In that setting, the object is a 1D vector of length M^2 , partitioned into M blocks of size M each. Again with $m = \lfloor \delta M \rfloor$, the measurement matrix A is $n = m \cdot M$ by $N = M \cdot M$, and has a block-diagonal form made of M blocks, each of size m by M . The off-diagonal blocks are all zero, and the diagonal blocks are random, filled with i.i.d. Gaussian entries

Figure 2 also shows the the finite- N phase transitions of block-diagonal undersampling schemes; we observe that the phase transition boundaries are visually indistinguishable from those of anisotropic undersampling, assuming the same value for the underlying δ .

²It will still be the case that at sufficiently large N , the shift goes away; however, it will become clear that the required N are unreasonably large, so such schemes in practice will always exhibit a noticeable shift, by an amount we here quantify precisely.

1.4 This paper’s contribution

This paper shows that the observed equality of phase transition between anisotropic undersampling and block-diagonal undersampling is no coincidence. We will demonstrate the formal equivalence of anisotropic undersampling with appropriate block-diagonal undersampling. We will then study block-diagonal undersampling carefully, and develop precise formulas for the finite- N phase transitions of sparse reconstruction from block-diagonal undersampling.

We have so far presented just the example of anisotropic undersampling in 2D Fourier imaging, but this is only a special case of our general results, which apply to fully general anisotropic undersampling of d -dimensional Fourier imaging, in which some dimensions are sampled uniformly at random and others are sampled exhaustively. In dimension $d = 2$ there is only one type of anisotropic sampling; but in higher dimensions one can have d_r dimensions sampled randomly and d_e dimensions sampled exhaustively, covering all $d = d_r + d_e$ dimensions. The case described so far is simply $d_r = 1, d_e = 1, d = 2$; but our results and methods are far more general.

An important conclusion from our study – see Corollary 10.1 – will be that, for a given number n of observations, the best sparsity-undersampling tradeoffs are obtained when d_e is as small as possible and d_r is as large as possible, in a way that we can quantify precisely. While that would seem to suggest always using $d_e = 0$ and hence using isotropic undersampling, in certain applications, randomness can only be implemented in a subset of the dimensions.

1.5 Application Areas

Our results apply to two important practical fields: MR imaging and NMR spectroscopy. In either setting, the experiment produces a sequence of *free induction decays* (FIDs); these are individual time series output by radio-frequency receivers. They are variously called repetitions, interleaves, or phase-encodes in MRI. In such a sequence the acquired data may be labeled $(k_0; k_1, \dots, k_{d-1})$, with k_0 indexing the time samples of the FID and (k_1, \dots, k_{d-1}) indexing the FID itself. Under complete acquisition, we would acquire a complete collection of FID’s, and thereby obtain a complete Cartesian sampling spanning $0 \leq k_i < M, i = 0, \dots, d - 1$, while under anisotropic undersampling, we would acquire only a subset of FID’s. In more detail:

- *Multi-dimensional MR imaging.* Ordinary MR imaging, producing a single 2D image, is effectively a case of $d = 2$ -dimensional Fourier imaging. Higher-dimensional MR imaging can be either 3D (x, y, z) or dynamic (t, x, y) or 3D dynamic (t, x, y, z) .

In MR imaging experiments, the FID $(\hat{x}_{k_0, \dots, k_{d-1}}, 0 \leq k_0 < M)$ can be viewed as the sequence of samples $(k_0, k_1, \dots, k_{d-1})$ for $0 \leq k_0 < M$ along a single line in the d -dimensional data hypercube of the traditional complex-valued d -dimensional Fourier transform.

Anisotropic undersampling has been used in some way in MRI for many years in some cases for the purpose of accelerating image acquisitions [28, 32, 31, 42, 39, 30, 23]. It has been called ‘random undersampling in the indirect dimensions or in the phase-encodes; see the article by Michael Lustig et al. [28].

- *Multi-dimensional NMR spectroscopy.* NMR spectroscopy experiments are more abstract and flexible than MR imaging, and can in principle be designed to encompass arbitrary-dimensional experiments; however, high-dimensional experiments take longer than low-dimensional ones, and practical limitations can intervene: these include denaturing of the sample material, and lack of exclusive access to a spectrometer for the days or weeks that might be required. In practice, experiments at higher dimensions than 3 are rarely attempted.

The FID in a spectroscopy experiment also can be viewed as the sequence of samples along a line in a d -dimensional data hypercube of ‘Fourier’ coefficients. However, the notion of Fourier transform differs in spectroscopy because each coefficient is hypercomplex-valued, so each sampled value $\hat{x}_{k_0, \dots, k_{d-1}}$ is 2^d -dimensional; for an explanation of this point see [36].

In NMR spectroscopy, anisotropic undersampling has been applied for decades by Jeffrey Hoch and collaborators; see [40, 41, 33, 24].

Mathematical scientists who study compressed sensing often mention MR imaging or NMR spectroscopy as applied settings where undersampled Fourier imaging is indeed applied successfully today; they rarely if ever mention that in either applied setting, the sampling is *always* anisotropic; it *never* makes sense to sample isotropically, because one *always* gets exhaustive samples along dimension k_0 inherently as part of the physical experiment; it makes no sense to throw away measurements that were already mandatorily taken. Mathematical scientists often speak as if

isotropic undersampling were an option in these applied settings, and reference theories involving isotropic undersampling. However, in either setting, isotropic sampling is not a sensible option, and the referenced theories do not offer accurate predictions of what happens in real experiments.

In contrast, our results describe anisotropic sampling of the type actually used in these applied fields and give accurate predictions of the sparsity/undersampling relation in undersampled imaging/spectroscopy.

1.6 Previous Work

Block-diagonal undersampling has been discussed in other applications of compressed sensing. For example, block-diagonal undersampling has been used for compressed image acquisition in [27, 18] and was studied as part of a more general category of compressed sensing, namely tensor compressed sensing, in [19, 26]. Also, Eftekhari et al. [16] study the Restricted Isometry Property (RIP) for block-diagonal matrices. Their study suggests that block-diagonal undersampling is qualitatively similar to dense Gaussian undersampling for compressed sensing.

In contrast, we consider precise finite- N phase transition properties and show that anisotropic undersampling has finite- N phase transitions different from the phase transitions for Gaussian undersampling. Our extensive computational results document the accuracy of our finite- N prediction formulas and show substantially worse phase transitions for anisotropic undersampling than for Gaussian undersampling. We do find that, asymptotically as N grows large, the finite- N phase transitions of anisotropic undersampling schemes converge to the asymptotic phase transition of Gaussian undersampling; however, this convergence occurs much more slowly than under isotropic sampling.³ Finally, this paper shows that certain instances of block-diagonal undersampling are equivalent to anisotropic undersampling in d -dimensional (hypercomplex-) Fourier imaging.

2 Finite- N Phase Transitions for Block Diagonal Measurements

In this section, we discuss the problem of recovering a sparse N -vector x_0 from n measurements $y = Gx_0$. The $n \times N$ measurement matrix G has a special block structure and we use a particular convex optimization in our attempt to recover x_0 . In one special case, we derive the exact finite- N phase transition properties and show that block-diagonal measurement matrices underperform dense *i.i.d.* Gaussian matrices by a substantial amount. In later sections, the *ansatz* provided by the explicit formulas derived in this special case are generalized to successfully predict experimental results across all other cases, with similar conclusions.

2.1 The convex optimization problem

The data vector y has been assumed to arise by applying the measurement matrix G to the unknown object x_0 . To reconstruct x_0 , we solve the following convex optimization problem:

$$(P_{1,\mathbf{X}}) \quad \min \|x\|_{1,\mathbf{X}} \quad \text{subject to} \quad Gx = y, \quad x \in \mathbf{X}^N.$$

Here each coefficient $x(i)$ is supposed to belong to a convex subset $\mathbf{X} \subset \mathbf{R}^d$ with nonempty interior, and $\|\cdot\|_{1,\mathbf{X}}$ denotes the (appropriately defined) “ ℓ_1 norm” on $(\mathbf{R}^d)^N$. The coefficient set \mathbf{X} might for example be $[0, 1]$, $[0, \infty)$, or \mathbf{R} , in which case $d = 1$ and $\|\cdot\|_{1,\mathbf{X}}$ denotes the usual ℓ_1 -norm on \mathbf{R}^N . But we could also have \mathbf{X} be $\mathbf{C} \subset \mathbf{R}^2$, or the 2^d -dimensional hypercomplex set $\mathbf{H}^d \subset \mathbf{R}^{2^d}$, in which case d is 2 or 2^d , and $\|\cdot\|_{1,\mathbf{X}}$ denotes what is more usually called the mixed $\ell_{2,1}$ norm: $\|x\|_{2,1} = \sum_{i=1}^N \|x(i)\|_{\ell_2(\mathbf{R}^d)}$.

Below, we often write (P_1) rather than $(P_{1,\mathbf{X}})$, making the coefficient domain explicit only where necessary.

³As an example, for an $M \times M$ grid where one of the dimensions is measured exhaustively, the rate of convergence is $M^{-1/2}$, while for a random sampling in both dimensions, this rate would be M^{-2} .

2.2 Block-Diagonal Measurement Matrices

In this section, the measurement matrices G will always be in block form:

$$G = \left[\begin{array}{c|c|c|c|c} A^{(1)} & 0 & 0 & \dots & 0 \\ \hline 0 & A^{(2)} & 0 & \dots & 0 \\ \hline & & \dots & & \\ \hline 0 & \dots & 0 & A^{(B-1)} & 0 \\ \hline 0 & \dots & 0 & 0 & A^{(B)} \end{array} \right],$$

where each block $A^{(b)}$ is $m \times M$. The 0's here also denote $m \times M$ blocks, filled with zero entries. The whole matrix is of size $n = mB$ by $N = MB$, and only the blocks on the diagonal can be nonzero.

We can construct such block diagonal matrices in two ways:

- *Repeated Block Ensembles (RB)*: Our blocks are simply B identical copies of the same $m \times M$ block.
- *Distinct Block Ensembles (DB)*: There are B distinct blocks of size $m \times M$.

To obtain the individual blocks, we often consider drawing them at random. A standard construction involves Gaussian *i.i.d* entries $A_{i,j} \sim N(0, \frac{1}{m})$. We often start with such a matrix but then normalize its columns to unit length; formalizing this:

Definition 3. A matrix A is said to (have columns sampled from, be sampled from) the Uniform Spherical Ensemble (USE) if its columns \mathbf{a}_i are sampled *i.i.d* from the uniform distribution on the unit sphere $S^{m-1} \subset \mathbf{X}^m$, where \mathbf{X} is either \mathbf{R} or \mathbf{C} .

Using random blocks from USE, the Distinct/Repeated blocks distinction gives us two kinds of matrix ensembles:

- *Repeated-Block USE (RBUSE)*. We draw a *single* block $A^{(1)}$ from USE. We generate a block-diagonal matrix $G = \text{diag}(A^{(1)}, \dots, A^{(1)})$ having all B blocks be identical copies of $A^{(1)}$. Equivalently, the full measurement matrix G is a *Kronecker* product: $G = I_B \otimes A^{(1)}$.
- *Distinct-Block USE (DBUSE)*. We draw B independently-sampled $m \times M$ blocks $A^{(b)}$, $b = 1, \dots, B$, from USE. We generate a block-diagonal matrix $G = \text{diag}(A^{(1)}, \dots, A^{(B)})$. This may equivalently be written as a direct sum: $G = \bigoplus_{b=1}^B A^{(b)}$.

3.1 Separability

Since our measurement matrix G has the block-diagonal form $G = \text{diag}(A^{(1)}, A^{(2)}, \dots, A^{(B)})$, it makes sense to partition the vectors y and x involved in the relation $y = Gx$ consistently with block structure of G :

$$x = [x^{(1)} \mid x^{(2)} \mid \dots \mid x^{(B)}], \quad y = [y^{(1)} \mid y^{(2)} \mid \dots \mid y^{(B)}],$$

where the subvectors $x^{(b)}$ are $M \times 1$, while the $y^{(b)}$ are $m \times 1$. The equation $y = Gx$ is then precisely equivalent to the B different relations

$$y^{(b)} = A^{(b)}x^{(b)}, \quad b = 1, \dots, B.$$

Define now the b -th *block subproblem*:

$$(P_1^{(b)}) \quad \min \|x\|_1 \quad \text{subject to} \quad A^{(b)}x = y^{(b)}, \quad x^{(b)} \in \mathbf{X}^M.$$

The key consequence of block-diagonality of G is that the optimization problem (P_1) becomes separable into its pieces $(P_1^{(b)})$.

Lemma 3.1. (Separability of (P_1)) We have

$$\text{val}(P_1) = \sum_{b=1}^B \text{val}(P_1^{(b)}).$$

Let $\mathcal{X}_1^{(b)} \subset \mathbf{X}^M$ denote the set of optimal solutions of $(P_1^{(b)})$ and let $\mathcal{X}_1 \subset \mathbf{X}^N$ denote the set of solutions of (P_1) . Then

$$\mathcal{X}_1 = \bigoplus_{b=1}^B \mathcal{X}_1^{(b)}.$$

In particular, suppose that each subproblem $(P_1^{(b)})$ has a unique solution $x_1^{(b)}$. The combined vector $x_1 = [x_1^{(1)} \mid x_1^{(2)} \mid \dots \mid x_1^{(B)}]$ is then the unique solution to (P_1) . Suppose that (P_1) has a unique solution x_1 . Then the b -th block of x_1 , say $x_1^{(b)}$, is the unique solution of $(P_1^{(b)})$.

Corollary 3.2. (Product rule for Success Probabilities) Suppose that the block matrices $A^{(b)}$, $b = 1, \dots, B$ are sampled i.i.d from a common distribution, and the subvectors $x_0^{(b)}$ are sampled i.i.d from a common distribution. Define the events

$$\Omega^{(b)} \equiv \{(P_1^{(b)}) \text{ has an unique solution } x_1^{(b)}, \text{ and } x_1^{(b)} = x_0^{(b)}\}$$

(i.e. $\Omega^{(b)} = \{\mathbf{x}_1^{(b)} = \{x_0^{(b)}\}\}$). Correspondingly, let

$$\Omega \equiv \{(P_1) \text{ has an unique solution } x_1, \text{ and } x_1 = x_0\}.$$

Then

$$\Omega = \bigcap_{b=1}^B \Omega^{(b)},$$

and

$$\Pr(\Omega) = \Pr(\Omega^{(1)})^B.$$

For clarity we point out that the matrices $A^{(b)}$ are not assumed by the Corollary to have any specific properties themselves, e.g. they do not have to have i.i.d elements $A_{ij}^{(b)}$; instead $A^{(i)}$ is simply assumed to be stochastically independent of $A^{(j)}$.

In a sense this corollary reduces the task of computing the probability of exact recovery to the task of computing $P(\Omega^{(1)})$.

3.2 Exact Finite- N Success Probabilities for $(P_{1,[0,1]})$

In one very special case, it is possible to evaluate $P(\Omega^{(1)})$ exactly at each M and ℓ . We study this case carefully for clues about the general situation. Consider the (single-block) convex optimization problem:

$$(P_{1,[0,1]}) \quad \min \|x\|_1 \quad \text{subject to} \quad Ax = y, \quad 0 \leq x(i) \leq 1.$$

This is an instance of what we earlier called $(P_{1,\mathbf{X}})$ with the specific coefficient set $\mathbf{X} = [0, 1]$. In this problem only, when we say that $y = Ax_0$ where x_0 has at most ℓ “nonzeros” we mean that at most ℓ coefficients $x_0(i)$ do not belong to the boundary $\{0, 1\}$ of $\mathbf{X} = [0, 1]$.

To proceed further, we need two notions:

- *Exchangeability.* The random variables Z_1, \dots, Z_M are *exchangeable* if, for any P on the set $\{1, \dots, M\}$, the joint probability distribution of $(Z_{P(1)}, \dots, Z_{P(M)})$ is the same as that for (Z_1, \dots, Z_M) .
- *General position.* The vectors $\mathbf{a}_1, \dots, \mathbf{a}_M$ are in *general position* in \mathbf{R}^m if no subcollection of at most m vectors is linearly dependent.

We now describe two conditions, either of which allows exact evaluation of success probabilities.

(C_A) A is any fixed $m \times M$ matrix with its M columns in general position in \mathbf{R}^m . x_0 is a random M -vector in $[0, 1]^M$ surely having ℓ entries different than 0 or 1, and the joint distribution of $(x_0(i) : 1 \leq i \leq M)$ is exchangeable.

(C_x) x_0 is any fixed vector in $[0, 1]^M$ having ℓ entries different than 0 or 1. A is a random $m \times M$ matrix whose columns $(\mathbf{a}^{(1)}, \mathbf{a}^{(2)}, \dots, \mathbf{a}^{(M)})$ are surely in general position and have an exchangeable joint distribution.

Theorem 3.3. [14] (**Exact Success probabilities in the Single-Block Problem, $\mathbf{X} = [0, 1]$.)** Assume either of assumptions (C_A) , (C_x) for the joint distribution of (A, x_0) . Let Ω denote the event that $(P_{[0,1]})$ has a unique solution, and that solution is precisely x_0 . Then $\Pr(\Omega)$ depends only on ℓ , m , M , and not on any other details of the joint distribution of (A, x_0) . In fact, $\Pr(\Omega) = Q_{SB}(\ell, m, M; [0, 1])$, where

$$\begin{aligned} Q_{SB}(\ell, m, M; [0, 1]) &= 1 - 2^{-(M-\ell-1)} \sum_{j=0}^{M-m-1} \binom{M-\ell-1}{j} \\ &= 1 - P_{M-m, M-\ell}, \text{ say.} \end{aligned} \quad (1)$$

We now remind the reader that in a sequence of B independent Bernoulli trials with common success probability q , the chance of B consecutive successes is q^B . As a result, we can infer general multiblock success probabilities from single-block ones (under appropriate assumptions).

Lemma 3.4. (Exact Success probabilities in the Multiblock Problem.) Consider a random instance of the multiblock problem $(P_{1, \mathbf{X}}^B)$, where the individual components $(A^{(b)}, x_0^{(b)})$ are i.i.d according to a specific distribution ν .

Let $Q_{SB} = Q_{SB}(\ell, m, M; \nu, \mathbf{X})$ denote the success probability for the single-block problem $(P_{1, \mathbf{X}}^{(1)})$: namely, let $\Omega^{(1)}$ denote the event that $(P_{1, \mathbf{X}}^{(1)})$ has a unique solution, and that solution is precisely $x_0^{(1)}$, and set

$$Q_{SB} = \Pr(\Omega^{(1)}).$$

Let $Q_{MB} = Q_{MB}(B \cdot \ell, B \cdot m, B \cdot M; \nu, \mathbf{X})$ denote the success probability for the multiblock problem $(P_{1, \mathbf{X}}^B)$: i.e., with $\Omega^{(B)}$ denoting the event that $(P_{1, \mathbf{X}}^B)$ has a unique solution, and that solution is precisely x_0 , we have

$$Q_{MB} = \Pr(\Omega^{(B)}).$$

Then

$$Q_{MB} = (Q_{SB})^B.$$

Turn now to the corresponding multiblock problem

$$(P_{1, [0,1]}^B) \quad \min \sum_{b=1}^B \|x^{(b)}\|_1 \quad \text{subject to} \quad A^{(b)} x^{(b)} = y^{(b)}, \quad 0 \leq x^{(b)}(i) \leq 1, \quad 1 \leq b \leq B.$$

Corollary 3.5. Consider a random instance of the multiblock problem $(P_{1, [0,1]}^B)$, where the individual components $(A^{(b)}, x_0^{(b)})$ are i.i.d according to a specific distribution ν that almost surely obeys (C_A) conditionally on A , or almost surely obeys (C_x) conditional on x_0 . Then when $N = B \cdot M$, $n = B \cdot m$, and $k = B \cdot \ell$,

$$Q_{MB}(k, n, N; \nu, [0, 1]) = Q_{SB}(\ell, m, M; [0, 1])^B. \quad (2)$$

Note that the RHS of (2) does not depend on any further details of the joint distribution ν . It is in this sense universal.

3.3 Finite- N Phase transition Location for $(P_{1, [0,1]}^B)$

We begin by defining the Finite- N phase transition in some generality.

Definition 4. Consider a random instance of an optimization problem (P) with problem sizes (k, n, N) , where n and N are the extent of the matrix G and k is the number of nonzeros in x_0 . Let $Q(k, n, N)$ denote the probability of success with given size parameters. Let k^* denote the smallest integer closest to achieving success probability $q^* = 1/2$:

$$Q(k^*, n, N) \approx \frac{1}{2}.$$

The Finite- N phase transition location is the ratio

$$\epsilon^*(n, N; (P)) = \frac{k^*}{N}.$$

We now apply this concept using the formulas of the last section, in two ways. Once, on a ‘classical’ single-block problem, and once on a multiblock problem of equivalent size.

- *Single-Block Problem.* Consider a single-block problem of size $N = BM$, $n = Bm$, $k = B\ell$, which is equivalent to the problem size of a multiblock problem to be considered next. We emphasize that this is not the main case for analysis in this section, but we study it for comparison purposes. It corresponds to the case $N = M$, $B = 1$ in our notation, which is not our usual case. Using the preceding Theorem, the critical number of nonzeros $k_{SB}^*(n, N)$ solves

$$Q_{SB}(k_{SB}^*, n, N) \approx q^*,$$

and we define the single-block Finite- N phase transition by

$$\epsilon_{SB}^* = \frac{k_{SB}^*(n, N)}{N}.$$

- *Multi-Block Problem.* Again in the multiblock setting $B \gg 1$, the preceding corollary shows that the probability of success is a function of ℓ, m, M, B . The critical number of nonzeros $\ell_{MB}^* = \ell_{MB}^*(m, M, B)$, yielding

$$Q_{SB}(\ell_{MB}^*, m, M)^B \approx q^*.$$

Setting $k_{MB}^* = B \cdot \ell^*$ for the equivalent total number of nonzeros and the total problem sizes $n = Bm$, $N = BM$, the phase transition location is

$$\epsilon_{MB}^*(m, M, B) = \frac{k_{MB}^*}{N} = \frac{B \cdot \ell^*}{B \cdot M} = \frac{\ell_{MB}^*(m, M, B)}{M}.$$

To be more concrete, we need specific assumptions about m, M , and B .

Lemma 4.1. *Consider a sequence of problem sizes where $B = M$, $M \rightarrow \infty$, and $m/M \rightarrow \delta \in (0, 1)$. With $N = B \cdot M$ and $n = B \cdot m$ we have $n \sim \delta N$. Define the asymptotic phase transition*

$$\epsilon^*(\delta; [0, 1]) = 2\delta - 1.$$

For the single-block finite- N phase transition we have:

$$\epsilon_{SB}^*(m, M; [0, 1]) = \epsilon^*(\delta) + O\left(\frac{1}{M}\right).$$

Define $\gamma_M = \sqrt{\frac{2 \log(M)}{M}}$. For the multi-block finite- N phase transition we have

$$\epsilon_{MB}^*(m, M, B; [0, 1]) = \epsilon^*(\delta) - \sqrt{2(1-\delta)} \cdot \gamma_M + O(\gamma_M^2).$$

Proof. See Appendix A. □

In particular, this lemma shows that as $B = M \rightarrow \infty$ with $m \sim \delta M$,

$$\epsilon_{SB}^*(m, M) - \epsilon_{MB}^*(m, M, B) = \sqrt{2(1-\delta)} \cdot \gamma_M \cdot (1 + o(1)).$$

While it may initially strike the reader that this shift in phase transitions locations is asymptotically negligible, observations—given above and also below—show it to be quite substantial in the intended applications. The mismatch between the single-block prediction and the observed behavior in the multiblock case is quite substantial unless M (not N) is large. In applications it is much harder to make M large than to make N large. Note that in the above lemma the system size is $N = BM = M^2$. Hence we may equivalently write

$$\epsilon_{SB}^* - \epsilon_{MB}^* \sim \frac{\sqrt{2(1-\delta) \log(N)}}{N^{1/4}}, \quad N \rightarrow \infty.$$

The denominator shows that the gap between the two phase transitions closes very slowly with increasing problem size N .

5 Equivalence with Anisotropic Undersampling

There is a precise equivalence between anisotropic undersampling and block-diagonal undersampling. We consider for now only the case of 2D Fourier imaging.

We wish to recover an unknown object $x_0 = (x_0(t_0, t_1) : 0 \leq t_i < M)$ with complex-valued entries, defined on a 2D grid of size $M \times M$. We assume that one acquires measurements of the form $y = \mathcal{A}x_0$, where \mathcal{A} is a pipeline of two linear operators. The first operator \mathcal{F}_2 is simply the usual complex-valued 2D finite Fourier transform that maps arrays in $\mathbf{C}^{M \times M}$ to their 2D DFT's, also in $\mathbf{C}^{M \times M}$. The second linear operator \mathcal{S}_2 is a random selection operator as described in the introduction, that takes as input an $M \times M$ array, samples m columns at random (say, columns $(k_i : 0 \leq i < m)$ where $0 \leq k_i < M$ and the k_i are all distinct). Within each selected column, it exhaustively samples all M elements. Then $\mathcal{A} = \mathcal{S}_2 \mathcal{F}_2$ implements anisotropic sampling in 2D-Fourier imaging.

For comparison, let $A^{(1)}$ denote an $m \times M$ block matrix representing the pipeline of two linear operators. The first, \mathcal{F}_1 , performs the usual 1D discrete Fourier transform of a vector $v \in \mathbf{C}^M$ delivering a transformed vector $\hat{v} \in \mathbf{C}^M$. The second, \mathcal{S}_1 , takes as input an M -vector (\hat{v} , say) and selects m entries ($\hat{v}_{k_i} : 1 \leq i \leq m$) out of the M indices available. It is important that the element indices (k_i) selected by \mathcal{S}_1 be *identical* to the column indices selected by the anisotropic selection operator \mathcal{S}_2 described earlier. Further, let A denote the block-diagonal matrix made by repeating the block matrix $A^{(1)}$ along the diagonal M times. Let $\mathbf{C}^{M \times M}$ denote the collection of arrays $x(t_0, t_1)$ with $0 \leq t_0, t_1 < M$, while \mathbf{C}^{M^2} denotes the collection of arrays $x(i)$ with $1 \leq i \leq M^2$.

Theorem 5.1. (Anisotropic undersampling models 2D Fourier Imaging.) *The following two problems have identical solution sets:*

$$\begin{aligned} (\text{Aniso}) \quad & \min \|x\|_{1, \mathbf{C}^{M \times M}} \quad \text{subject to} \quad \mathcal{A}x = y, \quad x \in \mathbf{C}^{M \times M}, \\ (P_{1, \mathbf{C}}) \quad & \min \|x\|_{1, \mathbf{C}^{M^2}} \quad \text{subject to} \quad Ax = y, \quad x \in \mathbf{C}^{M^2}. \end{aligned}$$

Proof. See Appendix B, which gives a much more general result of this kind. \square

We point out a very special variant that connects to earlier result.

Corollary 5.2. (Anisotropic undersampling in 2D Fourier Imaging, positive real coefficients.) *The following two problems have identical solution sets:*

$$\begin{aligned} (\text{Aniso}) \quad & \min \|x\|_{1, \mathbf{R}^{M \times M}} \quad \text{subject to} \quad Ax = y, \quad x \in [0, 1]^{M \times M}, \\ (P_{1, [0, 1]}^M) \quad & \min \|x\|_{1, \mathbf{R}^{M^2}} \quad \text{subject to} \quad Ax = y, \quad x \in [0, 1]^{M^2}. \end{aligned}$$

Lemma 5.3. (T. Tao) [44] *Suppose that M is prime. Then the $m \times M$ matrix A constructed above has its columns in general position in \mathbf{C}^m .*

Corollary 5.4. *Let M be prime. Let w_0 be a random vector of length $N = M^2$ with exactly ℓ nonzeros in each M -block. Let x_0 be a random vector created by randomly permuting the entries in each M -block, via uniformly-distributed random permutations that are stochastically independent from block to block.*

With G the fixed block matrix created above, and x_0 the random vector described in this Corollary, the assumptions (C_x) and general position of Corollary 3.4 apply. Hence the probability that the solution x_1 of the multiblock problem $(P_{1, [0, 1]}^M)$ is identical to x_0 is precisely given by the formula

$$\Pr(\{x_0 = x_1\}) = Q_{SB}(\ell, m, M; [0, 1])^M.$$

In consequence, our earlier results for block-diagonal undersampling give exact results for success probabilities in anisotropic undersampling. Let $\epsilon_{\text{aniso}}(m, M)$ denote the associated finite- N phase transition for exact recovery in anisotropic undersampling of the object x_0 in 2D-Fourier imaging.

Corollary 5.5. *Let x_0 be the random object constructed in the previous corollary. Let \tilde{G} denote an i.i.d Gaussian sensing matrix of size $n \times N$ and let $\tilde{y} = \tilde{G}x_0$ denote Gaussian undersampled measurements. Define*

$$(\tilde{P}_{1, [0, 1]}) \quad \min \|x\|_{1, \mathbf{C}} \quad \text{subject to} \quad \tilde{G}x = \tilde{y}, \quad x \in [0, 1]^N.$$

Let $\epsilon_{\tilde{G}}(n, N)$ denote the associated finite- N phase transition for exact recovery from Gaussian undersampling. Then we have, as M increases, the gap between Gaussian and anisotropic undersampling phase transitions has the following behavior:

$$\epsilon_{\tilde{G}}(mM, M^2) - \epsilon_{\text{aniso}}(m, M) = \sqrt{2(1 - \delta)} \cdot \gamma_M + O(\gamma_M^2).$$

6 Experimental Approach

The preceding section precisely locates the finite- N phase transition from anisotropic undersampling in one specific case. The finite- N phase transition is displaced downwards from the asymptotic phase transition by a definite amount, which depends on δ and M .

This formula can be generalized to apply across a wide range of situations, including general d -dimensional anisotropic sampling and encompassing coefficients that are real, complex and hypercomplex. In all these cases, the phase transition for anisotropic undersampling is substantially displaced from the phase transition for Gaussian undersampling, by an amount that matters in practically-important problem sizes. The scaling of this displacement with M and B is always the same, and the dependence on δ involves in a very particular way the underlying coefficient set \mathbf{X} .

To document these facts, we developed a framework for massive empirical simulation, which ultimately involved millions of computational experiments. Empirical results are more informative for applications than mathematical proofs would be, as they concern behavior in situations of the scale and type that one might actually encounter, instead of the very large problem sizes typically assumed by asymptotic mathematical analysis, which happen beyond the reach of modern computers and modern NMR experimentation. Our computational framework is consistent with the approach developed in [13, 37].

Though our computational setup allows for an arbitrary number of blocks, in this paper we present results only for the case of $B = M$, which as we have seen corresponds to the 2D-Fourier imaging.

6.1 Predictions of Phase Transition Location

Our formulas for the finite- N phase transition location in block-diagonal undersampling will be stated in terms of deviation from the asymptotic phase transition for Gaussian undersampling. We first make clear what this means, and then we state our formulas.

Formulas for Gaussian Phase Transition. We extend the discussion of Gaussian undersampling from Corollary 5.5, to cover situations of greater generality. Let the $n \times N$ random measurement matrix \tilde{G} have *i.i.d* $N(0, 1)$ entries⁴. For an object $x_0 \in \mathbf{X}^N$, we obtain n measurements $\tilde{y} = \tilde{G}x_0$. We attempt reconstruction via

$$(\tilde{P}_{1, \mathbf{X}}) \quad \min \|x\|_{1, \mathbf{X}} \quad \text{subject to} \quad \tilde{G}x = \tilde{y}, \quad x \in \mathbf{X}^N.$$

To predict success or failure, we take an asymptotic approach. Consider a sequence of problems indexed by $N \rightarrow \infty$ with $n/N \rightarrow \delta \in (0, 1)$, and in each problem instance let x_0 be k_N -sparse, where $k_N/N \rightarrow \epsilon \in (0, 1)$. Let \tilde{x}_1 denote the solution of $(\tilde{P}_{1, \mathbf{X}})$ with problem instance (\tilde{G}, \tilde{y}) . The existing literature on compressed sensing gives formulas for the critical sparsity level $\epsilon^*(\delta; \mathbf{X})$ such that, as $N \rightarrow \infty$,

$$\Pr\{\tilde{x}_1 = x_0\} \rightarrow \begin{cases} 1 & \epsilon < \epsilon^*(\delta; \mathbf{X}) \\ 0 & \epsilon > \epsilon^*(\delta; \mathbf{X}) \end{cases}.$$

For different choices of \mathbf{X} one can find such formulas in [10, 9, 8, 6, 2]. For example we have already used above the formula $\epsilon^*(\delta; [0, 1]) = (2\delta - 1)_+$.

Formula for regular sparsity. Now return to the block-diagonal undersampling case, where $N = MB$ and the measurement matrix G is block-diagonal, made from B different $m \times M$ blocks. We can partition the underlying vector $x_0 \in \mathbf{X}^N$ into B blocks of size M consistent with those of G . We say that x_0 has *regular sparsity* if it has the same number, ℓ say, of nonzeros in each block. We further assume that x_0 is random, with a block-exchangeable distribution. In this setting our formula states that observed solution to $(P_{1, \mathbf{X}})$ will exhibit, as a function of (\mathbf{X}, m, M, B) , a finite- N phase transition $\epsilon^r(m, M, B; \mathbf{X})$. Under the assumption that $M \rightarrow \infty$ and $m/M \rightarrow \delta \in (0, 1)$, the predicted displacement of the anisotropic undersampling phase transition $\epsilon^r(m, M, B; \mathbf{X})$ ‘below’ the Gaussian transition $\epsilon^*(m/M)$ obeys

$$\frac{\epsilon^*(\delta) - \epsilon^r(m, M, B)}{\epsilon^*(\delta)} = \alpha \cdot \eta(\delta) \cdot \gamma + O(\gamma^2), \quad (3)$$

⁴Exactly what this means can be spelled out more precisely in the case of Quaternionic or hypercomplex entries, although we do not pause to do so here.

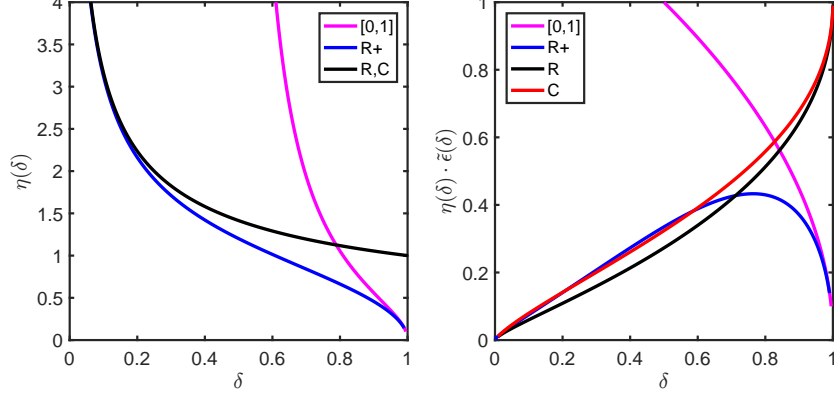


Figure 3: Slope functions in the finite-N prediction formula (3): (left) $\eta(\delta)$, (right) $\eta(\delta) \cdot \epsilon^*(\delta)$

where $\delta = n/N$, $\gamma = \gamma_{M,B} = \sqrt{2 \log(B)}/M$, $\alpha = \alpha_{\mathbf{X}}$ is a constant given in Table 1 below, and

$$\eta(\delta; \mathbf{X}) = \begin{cases} \epsilon^*(\delta)^{-1} (1 - \epsilon^*(\delta))^{\frac{1}{2}}, & \mathbf{X} = [0, 1] & \delta \in (\frac{1}{2}, 1] \\ \delta^{-\frac{1}{2}} (1 - \epsilon^*(\delta))^{\frac{1}{2}}, & \mathbf{X} = \mathbf{R}_+ & \delta \in (0, 1] \\ \delta^{-\frac{1}{2}}, & \mathbf{X} \in \{\mathbf{R}, \mathbf{C}\} & \delta \in (0, 1] \end{cases}.$$

Modeling the second order effect. When problem sizes are very small (e.g., $M = B = 100$), including the second-order effect in equation 3 leads to improved predictions of phase transitions, as will be evident from the plots of Section 7.2. We model the second-order effect by

$$\frac{\epsilon^*(\delta) - \epsilon^r(m, M, B)}{\epsilon^*(\delta)} = \alpha \cdot \eta(\delta) \cdot \gamma + \beta \cdot \zeta(\delta) \cdot \gamma^2 + o(\gamma^2), \quad (4)$$

where $\beta = \beta_{\mathbf{X}}$ is a constant given in Table 1, and

$$\zeta(\delta; \mathbf{X}) = \begin{cases} 1, & \mathbf{X} = [0, 1] & \delta \in (\frac{1}{2}, 1] \\ \eta(\delta; \mathbf{X}), & \mathbf{X} \in \{\mathbf{R}_+, \mathbf{R}, \mathbf{C}\} & \delta \in (0, 1] \end{cases}.$$

Table 1: Values for $\alpha_{\mathbf{X}}$ and $\beta_{\mathbf{X}}$ used in (4)

\mathbf{X}	[0, 1]	\mathbf{R}_+	\mathbf{R}	\mathbf{C}
$\alpha_{\mathbf{X}}$	1	1	1	2/3
$\beta_{\mathbf{X}}$	1/2	-1/3	-1/2	-1/3

6.2 Experimental Procedure

For each quadruple (k, m, M, B) , and each relevant coefficient ground set \mathbf{X} we run S Monte Carlo trials. In each experiment, we generate a pseudo-random k -sparse object $x_0 \in \mathbf{X}^N$ according to the regularity constraint \mathcal{RC} . We take undersampled linear measurements, $y = Gx_0$ where the B blocks of matrix G are each of size $m \times M$ and generated according to a certain random or deterministic sequence. (y, G) provides an instance of $(P_{1,\mathbf{X}})$ that we

supply to a convex optimization solver to obtain solution x_1 . We then compare x_0 with x_1 . If the relative error $\|x_0 - x_1\|_2 / \|x_0\|_2 < 0.001$, we declare the reconstruction a success; otherwise we declare it a failure. We thus obtain S binary measurements Y_i indicating success or failure of reconstruction. The empirical success probability is then calculated as

$$\hat{\pi}(k|G, \mathbf{X}, \mathbf{rc}) = \frac{\#\text{successes}}{\#\text{trials}} = M^{-1} \sum_{i=1}^M Y_i.$$

Our raw dataset contains these empirical success fractions, at each combination of (k, m, M, B, S) we explored.

6.3 Modeling the Quantal Response Function

In biological assessment, the quantal response measures the probability of organism failure (e.g., death) as a function of drug dose. In the context of compressed sensing, the quantal response gives the probability of failure in reconstruction as a function of the ‘complexity dose’, i.e. the number of nonzeros in the vector x_0 . This of course is measured by sparsity ratio ϵ . It is shown in [13] that a Probit model adequately describes the quantal response for Gaussian measurement matrices.

For block-diagonal matrices with block-regular sparsity, the failure probability is expected to follow the generalized extreme value distribution, as it involves the product of failure probabilities of individual blocks. Extreme value theory shows that for large B , the Complementary Log Log (CLL) distribution is an appropriate model for quantal response. Given certain problem size (M, B) , that theory states that the expected fractional success rate can be modeled as

$$\pi(\epsilon|\delta) = \Pr\{\text{Success}|\delta, \epsilon\} = 1 - \exp\{-\exp(a(\delta) + b(\delta) \cdot \epsilon)\}, \quad (5)$$

for certain underlying parameters $a = a(\delta)$, and $b = b(\delta)$. We then define the empirical phase transition location, at each fixed δ , as the sparsity level ϵ at which the success probability $\pi = 1 - 1/e$ (i.e., 63.2%).

6.4 Studying Very Large Problem Sizes

In the results sections we attempt to get a clear understanding of models explaining displacements of order γ and γ^2 . This required data from experiments conducted at a range of problem sizes - in particular large problem sizes. Actually, plausible sizes can easily lead to computational difficulties. In a 2D anisotropic undersampling problem on a 768×768 Fourier grid, we would be considering block-diagonal undersampling with parameters $M = B = 768$, in which case $N = 768^2 = 589824$. General-purpose convex optimization solvers such as CVX are not really appropriate for solving such large problems.

Nevertheless, we have been able to get precise information about the behavior of $(P_{1,\mathbf{X}})$ on block-diagonal problems of such large sizes. The key comes in applying Lemma 3.4, which allows us to infer success probabilities for problems of size $N = B \cdot M$, once we know them for problems of size M . In the cases we are studying, $B = M$, so $M = \sqrt{N}$ and we can use computationally modest resources to study problems that would ordinarily require massive investments of computational resources.

Let $Q_{MB}(k, n, N; \nu, \mathbf{X})$ denote the probability of success in the multiblock optimization problem $(P_{1,\mathbf{X}}^B)$ at given $k = B \cdot \ell$, $n = Bm$ and $N = BM$, where the component subproblems are *i.i.d* according to a fixed distribution ν . Let $Q_{SB} = Q_{SB}(\ell, m, M; \nu, \mathbf{X})$ denote the probability of success in a component single-block problem. Lemma 3.4 gives us the equivalence:

$$Q_{MB}(k, n, N) \leq q^* \Leftrightarrow Q_{SB}(\ell, m, M) \leq (q^*)^{1/B}.$$

At first blush, a hypothesis on Q_{MB} —such as the finite- N phase transition—would seem to require evidence from trials in which the multiblock problem $(P_{1,\mathbf{X}}^B)$ of total size $N = B \cdot M$ gets solved. But we have just shown that such a hypothesis on Q_{MB} is equivalent to one on Q_{SB} . We get information about Q_{SB} by solving random instances of a single-block problem of size M . Suppose $k = B \cdot \ell$ and $N = BM$. Then the hypothesis that $\epsilon_{MB}^* < k/N$ is equivalent to $Q_{MB}(k, n, N) < q^*$, which is equivalent to $Q_{SB}(\ell, m, M) < (q^*)^{1/B}$. So we can indeed use single-block problem realizations to shed light on ϵ_{MB}^* .

Generate S independent problem realizations $(A^{(s)}, x_0^{(s)})$, each one a single-block problem instance with size parameters ℓ, m, M . Solve each realization in turn and record the binary success indicators $X_s = 1_{\{x_1^{(s)} = x_0^{(s)}\}}$. These are Bernoulli random variables at some common but unknown success probability, π , say. Let $Y_s = 1 - X_s$ denote the indicator of failure. Calculate the mean failure rate $\bar{Y} = S^{-1} \sum_{s=1}^S Y_s$.

We propose the following (approximate) level α test of $H_0 : (1 - \pi)^B \leq q^*$ against $H_1 : (1 - \pi)^B > q^*$. Define $\mu = \mu_B = \log(1/q^*)/B$. Reject the hypothesis H_0 if the failure fraction is high:

$$\bar{Y} > \mu + z_{1-\alpha/2} \sqrt{\frac{\mu}{S}}.$$

Accept H_0 if the fraction of failures is low:

$$\bar{Y} < \mu - z_{1-\alpha/2} \sqrt{\frac{\mu}{S}}.$$

Derivation: Let $q_B = 1 - (q^*)^{1/B}$, and suppose our variables were distributed as $X_s \sim \text{Ber}((q^*)^{1/B})$, i.e., just on the sharp edge of the phase transition at problem size B . Then $Y_s \sim \text{Ber}(q_B)$. Let $T = \sum_{s=1}^S Y_s$; then $T \sim_{\text{approx}} \text{Poi}(\lambda)$, where $\lambda = S \cdot \mu$. By normal approximation to the binomial, when λ is large, $T \sim_{\text{approx}} N(\lambda, \lambda)$. Consequently,

$$\Pr\{T \in [\lambda - z_{1-\alpha/2} \sqrt{\lambda}, \lambda + z_{1-\alpha/2} \sqrt{\lambda}]\} \approx 1 - \alpha,$$

where the approximation gets increasingly good as $\lambda \rightarrow \infty$. The rule we proposed above then follows.

Another way to write the rule sets $T = S \cdot \bar{Y}$. Then we can decide to reject/accept just in case

$$\bar{Y} \notin \mu \cdot \left(1 \pm \frac{z_{1-\alpha/2}}{\sqrt{S \cdot \mu}} \right).$$

The probability of mistaken rejection is approximately α .

7 Results

7.1 Data collection

To efficiently generate the quantal response data for various ensembles, we have developed and used software package Clusterjob (CJ) [34] - a collection of Perl scripts for automating reproducibility and hassle-free submission of massive computational jobs to clusters. Our computational jobs have mainly run on three different clusters at Stanford, namely `sherlock`, `solomon`, and `proclus`. The optimization solvers used include ASP[20, 21], CVX [22], and MOSEK[1]. It is worth mentioning that software package CVX uses SDPT3 and SEDUMI as its main optimization solvers. Our dataset currently includes 29 million rows, which are the results of nearly 35 million Monte Carlo runs for various problem sizes, and ensembles including RBUSE, DBUSE, RBPFT, etc. For experiments involving smaller problem sizes, one row of data contains information such as the probability of successful reconstruction and error in reconstruction for a particular quadruple (ℓ, m, M, B) in the phase space. For data of larger problem sizes, one row contains information such as error in reconstruction and a binary number indicating success or failure for a particular triple (ℓ, m, M) .

7.2 Verifying predictions

Figures 4 through 14 show the comparison of experimental phase transition data against the first-order and second-order predictions for the four different coefficient sets $\mathbf{X} \in \{[0, 1], \mathbf{R}_+, \mathbf{R}, \mathbf{C}\}$. As an example, Figure 4 shows the empirical offset from the asymptotic phase transition location and the corresponding predictions for recovering a bounded object, for which exact rigorous results were presented in Section 4. In all these cases, the match between the the predictions and data is clear. The figures also show that the second-order correction terms improve the predictions of the phase transition location - especially for smaller problem sizes.

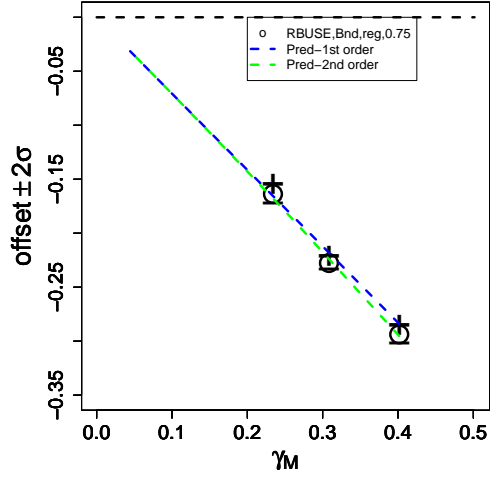


Figure 4: Displacement $\epsilon^* - \epsilon_M$ as a function of γ_M for RBUSE ensemble and $\mathbf{X} = [0, 1]$ at $\delta = 3/4$. Problem sizes: $N = 48, 96$ and 192 . The green and blue curves show the predictions with and without considering the second-order effects, respectively.

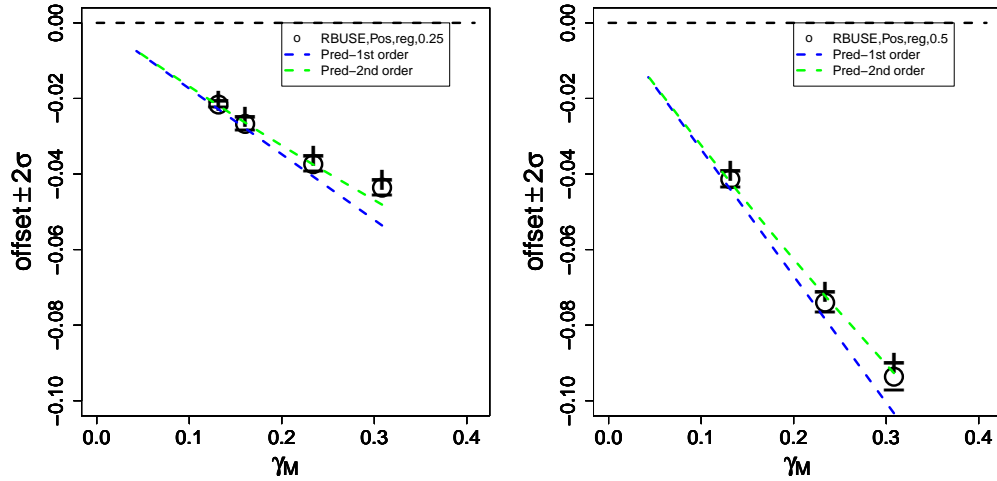


Figure 5: Displacement $\epsilon^* - \epsilon_M$ as a function of γ_M for RBUSE ensemble and $\mathbf{X} = \mathbf{R}_+$ at $\delta = 1/2$ (left panel) and $\delta = 1/4$ (right panel). Problem sizes: $M = 96, 192, 480$ and 768 . The green and blue curves show the predictions with and without considering the second-order effects, respectively.

+ Positive Coefficients

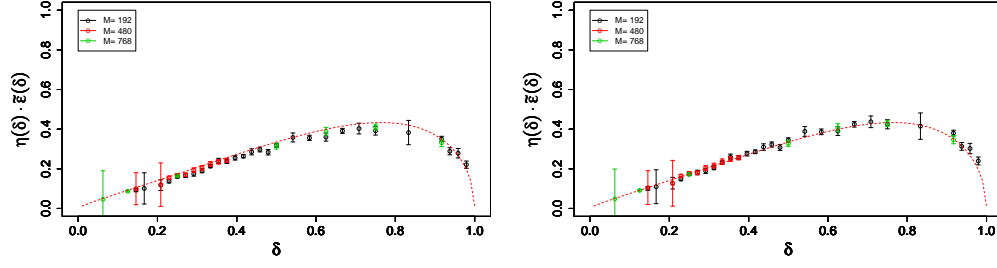


Figure 6: The ratio of displacement $\epsilon^* - \epsilon_M$ to $\alpha\gamma_M$ (left panel-first order) and $(\alpha\gamma_M + \beta\gamma_M^2)$ (right panel-second order) as a function of undersampling δ for RBUSE ensemble and $\mathbf{X} = \mathbf{R}_+$ coefficient set. Problem sizes: $M = 192, 480$ and 768 . The red dashed curve shows the predictive curves $\eta(\delta) \cdot \epsilon(\delta)$.

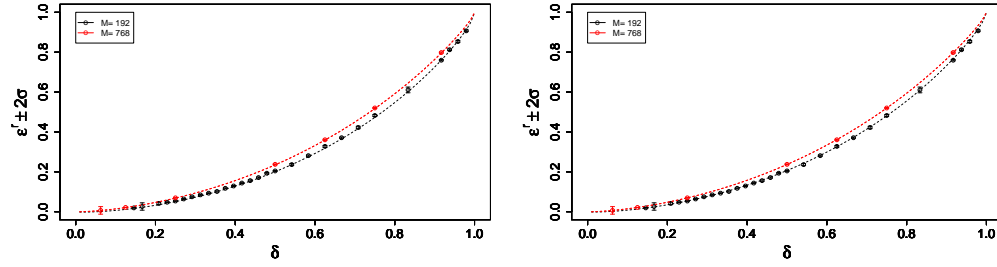


Figure 7: Experimental data against first-order (left), and second-order (right) predictions of phase transition for $\mathbf{X} = \mathbf{R}_+$. Problem sizes: $M = 192, 768$. The circles are data and the dashed lines are predictions.

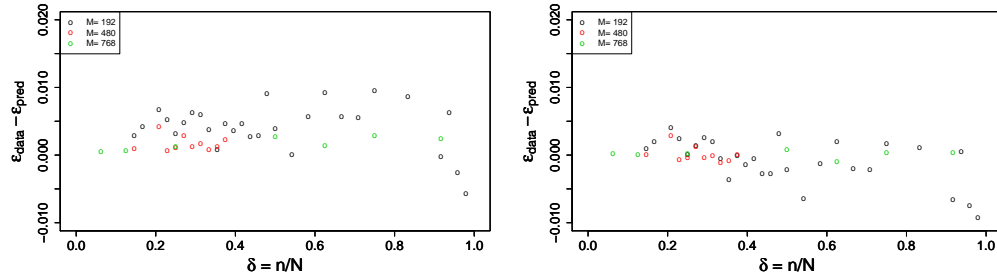


Figure 8: Difference of predicted and experimental phase transition location for $\mathbf{X} = \mathbf{R}_+$ using first-order (left), and second-order (right) predictive models. Problem sizes: $M = 192, 480$ and 768 . Residuals are larger near $\delta \approx 1$, the residuals at $M = 768$ and large δ are noticeably smaller than those at $M = 192$.

+ Real Coefficients

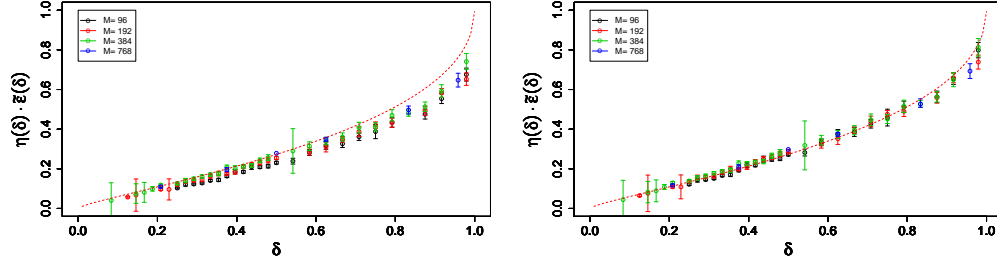


Figure 9: The ratio of displacement $\epsilon^* - \epsilon_N$ to $\alpha\gamma_M$ (left panel-first order) and $(\alpha\gamma_M + \beta\gamma_M^2)$ (right panel-second order) as a function of undersampling δ for RBUSE ensemble and $\mathbf{X} = \mathbf{R}$. Problem sizes $M = 96, 192, 384$ and 768 . The red dashed curve shows the predicted curves $\eta(\delta) \cdot \epsilon(\delta)$.

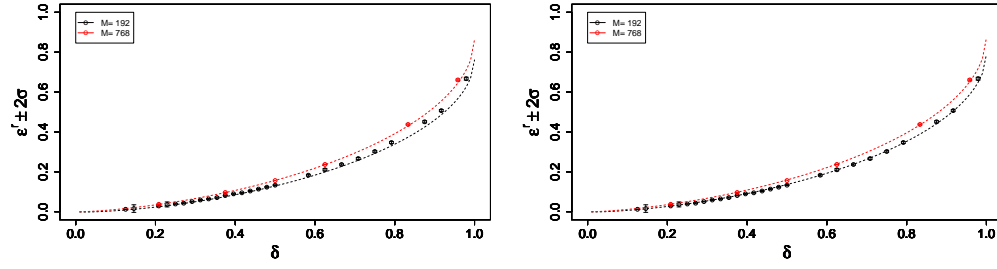


Figure 10: Experimental data against first-order (left), and second-order (right) predictions of phase transition for $\mathbf{X} = \mathbf{R}$. Problem sizes: $M = 192, 768$. The circles are data and the dashed lines are predictions.

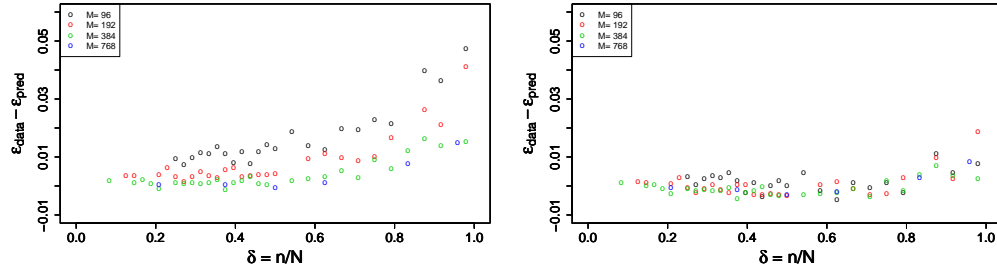


Figure 11: Difference of predicted and experimental phase transition location for $\mathbf{X} = \mathbf{R}$ using first-order (left), and second-order (right) predictive models. Problem sizes $M = 96, 192, 384$ and 768 . Residuals are larger near $\delta \approx 1$, the residuals at $M = 768$ and large δ are noticeably smaller than those at $M = 96$.

+ Complex Coefficients

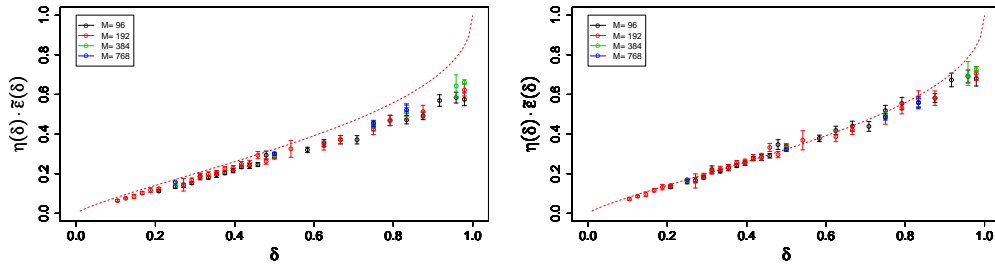


Figure 12: The ratio of displacement $\tilde{\epsilon} - \epsilon_N$ to $\alpha\gamma_M$ (left panel-first order) and $(\alpha\gamma_M + \beta\gamma_M^2)$ (right panel-second order) as a function of undersampling δ for RBUSE ensemble and $\mathbf{X} = \mathbf{C}$. Problem sizes $M = 96, 192, 384$ and 768 . The red dashed curve shows the predictive curves $\eta(\delta) \cdot \epsilon(\delta)$.

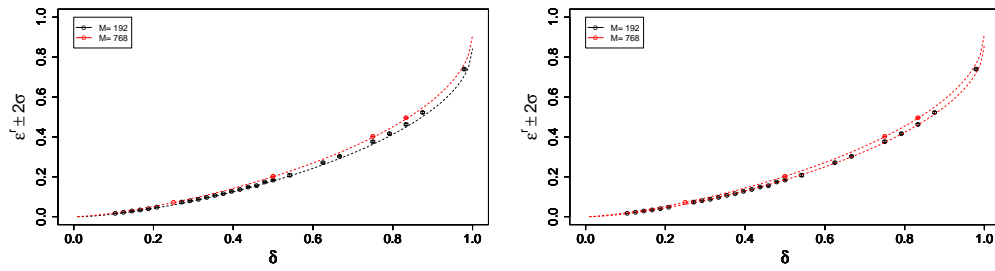


Figure 13: Experimental data against first-order (left), and second-order (right) predictions of phase transition for $\mathbf{X} = \mathbf{C}$. Problem sizes: $M = 192, 768$. The circles are data and the dashed lines are predictions.

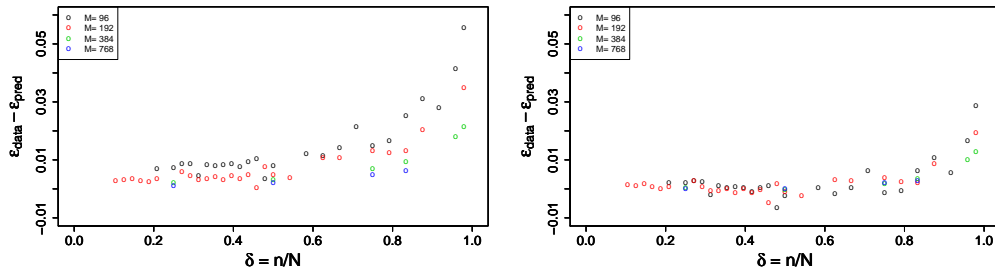


Figure 14: Difference of experimental and predicted phase transition location for $\mathbf{X} = \mathbf{C}$ using first-order (left), and second-order (right) predictive models. Problem sizes $M = 96, 192, 384$ and 768 . Residuals are larger near $\delta \approx 1$, the residuals at $M = 768$ and large δ are noticeably smaller than those at $M = 96$.

8 Stylized Application to MR Imaging

Numerous researchers [46, 48, 47, 43, 17] have been conducting MR imaging experiments where one dimension is sampled exhaustively and the others are sampled at random, and in some cases uniformly at random exactly as discussed here; see for example [28].

Theorem 5.2 shows that the $2D$ Fourier imaging with anisotropic undersampling is equivalent to block-diagonal measurements with $B = M$ and $N = M^2$. This equivalence is illustrated in Figure 2. As expected, the empirical phase transition of the anisotropically-undersampled $2D$ FT is substantially below the transition point for Gaussian measurement matrices.

The $2D$ imaging situation corresponds to the case where $\mathbf{X} = \mathbf{C}$. and $\gamma_M = \sqrt{2 \log(M)/M}$. In the case of $\|\cdot\|_{1,\mathbf{C}}$ minimization our formulas give the following displacement between the asymptotic phase transition and the finite- N transition:

$$\begin{aligned} \text{displacement} &\sim \alpha_{\mathbf{C}} \cdot \eta(\delta; \mathbf{C}) \cdot \gamma_M + \beta_{\mathbf{C}} \cdot \zeta(\delta; \mathbf{C}) \cdot \gamma_M^2 + o(\gamma_M^2) \\ &= \delta^{-1/2} \left[\frac{2}{3} \gamma_M - \frac{1}{3} \gamma_M^2 \right] + o(\gamma_M^2) \\ &= \delta^{-1/2} \left[\frac{2\sqrt{2}}{3} \sqrt{\frac{\log(M)}{M}} - \frac{2}{3} \frac{\log(M)}{M} \right] + o\left(\frac{\log(M)}{M}\right). \end{aligned}$$

The experiments reported here validated the formalism's predictions, which can thus be used to gauge the amount of undersampling required in $2D$ imaging experiments.

Lustig and Pauly [28] also proposed anisotropic undersampling for $3D$ MR imaging, where one dimension is acquired exhaustively and the other two are acquired uniformly at random [28]. Our formalism applies to $3D$ MR imaging, where $\mathbf{X} = \mathbf{C}$, $B = M$, $N = M^3$, and $\gamma_M = \sqrt{2 \log(M)/M^2}$.

$$\begin{aligned} \text{displacement} &\sim \alpha_{\mathbf{C}} \cdot \eta(\delta; \mathbf{C}) \cdot \gamma_M + \beta_{\mathbf{C}} \cdot \zeta(\delta; \mathbf{C}) \cdot \gamma_M^2 + o(\gamma_M^2) \\ &= \delta^{-1/2} \left[\frac{2}{3} \gamma_M - \frac{1}{3} \gamma_M^2 \right] + o(\gamma_M^2) \\ &= \delta^{-1/2} \left[\frac{2\sqrt{2}}{3} \frac{\sqrt{\log(M)}}{M} - \frac{2}{3} \frac{\log(M)}{M^2} \right] + o\left(\frac{\log(M)}{M^2}\right). \end{aligned}$$

The leading term involves $1/M = 1/N^{1/3}$ in the $3D$ case, replacing the leading term $1/\sqrt{M} = 1/N^{1/4}$ from the $2D$ case.

9 Stylized Application to MR Spectroscopy

Jeffrey Hoch and collaborators have used anisotropic random undersampling in multi-D NMR spectroscopy for more than two decades [40]. In MR Spectroscopy, anisotropic undersampling is not the full story; we must also consider the Hypercomplex nature of object \mathbf{x} .

A d -dimensional experiment collects measurements on an array \mathbf{x} indexed by a d -dimensional grid of size $T_0 \times \dots \times T_{d-1}$, and having hypercomplex entries. Each hypercomplex entry is a 2^d -dimensional vector over the real field \mathbf{R} . Traditionally, the complete set of measurements in MR spectroscopy is a set of $2^{d-1} \cdot \left(\prod_{1 \leq i < d} T_i \right)$ FID's; different FIDs are indexed by $(\ell; k_1, \dots, k_{d-1})$. Each FID $F_{k_1, \dots, k_{d-1}}^\ell(\cdot)$ is a complex-valued time series ($F_{k_1, \dots, k_{d-1}}^\ell(k_0) : 0 \leq k_0 < T_0$) and measures two real coordinates of the hypercomplex entry associated with site $(k_0, k_1, \dots, k_{d-1})$ as k_0 varies, effectively sampling along an axis-oriented line $k_0 \mapsto (k_0, k_1, \dots, k_{d-1})$ in $\mathbf{Z}_{T_0} \times \dots \times \mathbf{Z}_{T_{d-1}}$. Traditional full acquisition requires 2^{d-1} full passes through the Cartesian grid, each pass - indexed by $\ell = 0, 1, \dots, 2^{d-1} - 1$ - measuring a different pair of coordinates of the full 2^d -dimensional entry associated with a given site.

In NMR spectroscopy, anisotropic undersampling is generally called *NUS* (for *non-uniform sampling*) [40]. To carry it out, simply sample uniformly at random without replacement from the set of tuples (k_1, \dots, k_{d-1}) and then collect 2^{d-1} FIDs at each such tuple - $\ell = 0, \dots, 2^{d-1} - 1$ - i.e. collecting each $F_{k_1, \dots, k_{d-1}}^\ell(\cdot)$ associated to each selected tuple. Theorem 5.2 can be generalized as follows, although we omit details in this article.

Theorem 9.1. (multi-D NUS) *Let $N = 2^d \prod_{i=0}^{d-1} T_i$ and suppose that n is divisible by $2^d T_0$. From the collection of tuples (k_1, \dots, k_{d-1}) in $\mathbf{Z}_{T_1} \times \dots \times \mathbf{Z}_{T_{d-1}}$, sample uniformly at random $n/(2^d \cdot T_0)$ such tuples. There is a*

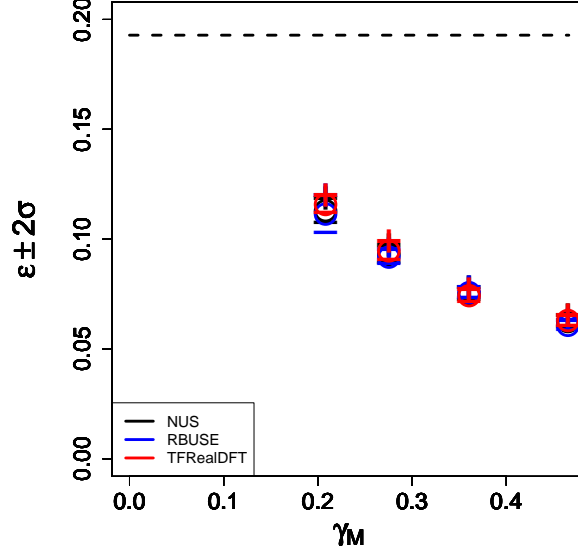


Figure 15: Equivalence of standard undersampling schemes in 2D MR Spectroscopy with anisotropic undersampling schemes involving block-diagonal measurements. The data come from a $T \times T$ Cartesian grid, amounting to $4T^2$ real coefficients. The undersampling fraction $\delta = 1/2$. ‘NUS’ models undersampling of the indirect dimension in MR Spectroscopy, selecting at random half of the $y = \text{constant}$ lines to be measured. ‘RBRealDFT’ corresponds to block-diagonal measurements with $B = 2T$ repeated blocks of size $T \times 2T$, each block the real representation of a partial 1D complex Fourier matrix, in which each complex entry is replaced by its equivalent 2×2 real matrix. ‘RBUSE’ corresponds to block-diagonal measurements with $2T$ identical blocks, each block an $T \times 2T$ real USE matrix. The dashed line represents the asymptotic Gaussian phase transition at $\delta = 1/2$. Problem sizes: $N = 16, 32, 64, 128$.

corresponding $n \times N$ block-diagonal matrix G with $B = T_0$ identical blocks; each block is a short fat real matrix of size $m \times M$ with $m = n/T_0$ and $M = N/T_0$. The following two problems have identical solution sets:

$$\text{(aniso)} \quad \min \|x\|_{1,\mathbb{C}} \quad \text{subject to} \quad Ax = y,$$

$$\text{(BD)} \quad \min \|x\|_{1,\mathbb{C}} \quad \text{subject to} \quad Gx = y.$$

For the special case of NUS in 2D experiments when only half of the indirect times are sampled (i.e., $\delta = 1/2$), the block diagonal matrix in Theorem 9.1 consists of $B = 2T$ repeated blocks of size $m \times M = T \times 2T$. Each repeated block is a real-valued matrix implementing a partial 1D complex discrete Fourier transform (in this representation, each complex entry in the complex DFT matrix is replaced by its equivalent 2×2 real matrix). We label this block diagonal matrix by ‘RBRealDFT’. The figure documents the equivalence of NUS with ‘RBRealDFT’. The figure also documents performance with the RBUSE block-diagonal measurement matrix where, in place of each partial Fourier Matrix we insert a random USE matrix. The results are similar; this is an instance of the universality phenomenon discovered in [11, 37].

10 The general multidimensional case

We will give a full report on the multidimensional case elsewhere, documenting the accuracy of the prediction formalism developed here. The key points can already be seen. Suppose the object of interest is a d -dimensional array, with sidelength T on each axis, so the total data volume $N = T^d$. In anisotropic undersampling of such an array, let $B = T^{d_e}$ where d_e is the number of exhaustively sampled dimensions; the individual blocks themselves are then of dimension $M = T^{d_r}$, where $d_r = d - d_e$. Our *ansatz* for the location of the finite-N phase transition in Lemma 4.1 translates to this special case as follows:

Corollary 10.1. (General $d \geq 2$). *Let $d \in \{2, 3, 4, \dots\}$, and fix $0 \leq d_e, d_r \leq d$, such that $d_r + d_e = d$. Consider a sequence of problem sizes $T \rightarrow \infty$ and associated block-diagonal matrices with $B = T^{d_e}$ blocks of equal size*

$m \times M$, and with $m/M \rightarrow \delta \in (0, 1)$. For the displacement between the asymptotic phase transition $\epsilon^*(\delta; [0, 1])$ and the multi-block finite- N phase transition $\epsilon^*(m, M, B; [0, 1])$ we have:

$$\epsilon^*(\delta) - \epsilon_{MB}^* \sim \sqrt{\frac{4 \frac{d_e}{d} (1 - \delta) \log(N)}{N^{d_r/d}}}, \quad N \rightarrow \infty.$$

Two comments are in order:

- Comparing two schemes with equivalent n/N and N , but different d_e , we see that this gap is increasing in the quantity d_e/d . In words: other things being equal, the gap is larger when there are more exhaustively sampled dimensions and hence fewer randomly sampled dimensions.
- Comparing two problems with the same d_e but different d , we see that the gap is relatively less important when d is larger. For example, in multidimensional MR spectroscopy, the gap between the asymptotic Gaussian-measurements phase transition and the finite- N phase transition is larger in smaller dimensions d than in larger dimensions. The order of the gap in 2D-MRI – where $d_e = 1$, $d_r = 1$ – is $O(\sqrt{\log(N)}N^{-1/4})$; while in 3D MRI – where $d_e = 1$, $d_r = 2$ – it is $O(\sqrt{\log(N)}N^{-1/3})$.

11 Conclusion

We formalized the notion of anisotropic undersampling in multi-dimensional Fourier imaging, and showed its mathematical equivalence with the use of block-diagonal measurement matrices in compressed sensing.

We rigorously analyzed a special case of block-diagonal measurement matrices where the object of interest has real coefficients bounded between 0 and 1 which are sparsely not at the extreme values 0 and 1, and derived a precise expression for the finite- N phase transition, finding it to be displaced substantially from the large- N phase transitions previously known for fully dense Gaussian measurement schemes. Indeed the displacement is so great that at practical-sized problems the asymptotic Gaussian predictions are simply not relevant.

Massive computational experiments involving millions of CPU hours established the empirical equivalence of random anisotropic Fourier undersampling with block diagonal Gaussian measurements. The experiments showed that the phenomenon of substantial finite- N phase transition displacement from the fully dense Gaussian measurement case – proven theoretically in the above special case – continues to hold empirically across a range of other settings, including the recovery of sparse objects with real coefficients, with real nonnegative coefficients or complex coefficients. The experiments allowed us to validate precise formulas for the finite N -phase transitions adapted to all those cases, including second-order [in γ] versions of our formulas matching the experimental data closely.

We presented formulas for the location of finite- N phase transitions in 2D and 3D Sparse MRI, where anisotropic undersampling has a long history and has been extensively used. We briefly discussed multi-dimensional MR spectroscopy, which involves anisotropic undersampling of the hypercomplex Fourier transform, and we empirically demonstrated its equivalence to block-diagonal Gaussian measurements in the 2D hypercomplex case. We left detailed discussion of the multidimensional hypercomplex case for future work.

Reproducible Research

The code and data that generated the figures in this article may be found online at <https://purl.stanford.edu/th702qm4100> [35].

A Proof of Lemmas 4.1 and 10.1

The success probability for the multi-block problem and regular sparsity is given by,

$$Q_{MB}(B \cdot \ell^*, B \cdot m, B \cdot M) = Q_{SB}(\ell^*, m, M)^B \approx q^*$$

where $Q_{SB}(\ell^*, m, M)^B = 1 - P_{M-m, M-\ell}$ as defined in Theorem 3.3.

We are interested in the setting where the number of blocks $B \rightarrow \infty$; since q^* is fixed, it follows that the success probability for individual blocks $Q_{SB}(\ell^*, m, M)$ is roughly $(q^*)^{1/B}$ and tends to 1, and the failure probability for individual blocks tends to zero. For large block sizes B , the failure probability for individual blocks $P_{M-m, M-\ell} \rightarrow 0$, and so we can use an approximation of the following form:

$$P_{M-m, M-\ell} = \frac{\log(1/q^*)}{B}.$$

The binomial distribution is approximated by a Gaussian distribution for suitably large problem sizes:

$$\begin{aligned} P_{M-m, M-\ell^*} &\approx \Phi\left(\frac{(M-m) - \left(\frac{M-\ell^*}{2}\right)}{\frac{\sqrt{M-\ell^*}}{2}}\right) \\ &= \Phi\left(\frac{M-2m+\ell^*}{\sqrt{M-\ell^*}}\right). \end{aligned} \quad (6)$$

Now, let $z_B = \Phi^{-1}\left(\frac{\log(1/q^*)}{B}\right)$. The precise finite- N phase transition location ℓ^* is found by solving,

$$\frac{M-2m+\ell^*}{\sqrt{M-\ell^*}} = z_B,$$

which leads purely formally to,

$$\ell^* = 2m - M - \frac{1}{2}\sqrt{z_B^4 + 8z_B^2(M-m) - \frac{z_B^2}{2}};$$

dividing both the sides by M and letting $\delta = m/M$:

$$\begin{aligned} \epsilon_{MB}^*(m, M, B, [0, 1]) &= 2\delta - 1 - \frac{1}{2}\sqrt{\left(\frac{z_B^2}{M}\right)^2 + \frac{8z_B^2(M-m)}{M^2} - \frac{z_B^2}{2M}} + O\left(\frac{1}{M}\right) \\ &= 2\delta - 1 - |z_B|\frac{\sqrt{2(1-\delta)}}{\sqrt{M}} + O\left(\frac{z_B^2}{M}\right) \\ &= \epsilon_{SB}^*(m, M; [0, 1]) - |z_B|\frac{\sqrt{2(1-\delta)}}{\sqrt{M}} + O\left(\frac{z_B^2}{M}\right). \end{aligned} \quad (7)$$

For B large, we use the following classical approximation to z_B :

$$|z_B| = \sqrt{2\log(B)} \cdot (1 + o(1)), \quad B \rightarrow \infty.$$

Setting $\gamma = \sqrt{\frac{2\log(B)}{M}}$ gives:

$$\epsilon_{MB}^*(m, M, B; [0, 1]) = \epsilon_{SB}^*(m, M; [0, 1]) - \sqrt{2(1-\delta)}\gamma + O(\gamma^2). \quad (8)$$

B Proof of Theorem 5.2

The proof of Theorem 5.2 relies on three lemmas.

Lemma B.1. (Rank-deficient matrix) Consider the rank-deficient $n \times N$ ($n < N$) measurement matrix G with $\text{rank}(G) = r < n$ and $x_0 \in \mathbf{R}^N$ generating measurements $b = Gx_0$. The minimum- ℓ_1 optimization problem

$$\min \|x\|_1 \quad \text{subject to} \quad Gx = b$$

has the same solution set as the reduced-dimensional problem

$$\min \|x\|_1 \quad \text{subject to} \quad Ax = y,$$

where A is a full-row-rank matrix of size $r \times N$ and $y = Ax_0$.

Proof. Using the SVD $G = U\Sigma V^T$, where $U \in R^{n \times r}$, $V \in R^{N \times r}$, and $\Sigma \in R^{r \times r}$. Then

$$\begin{aligned} Gx &= b, \\ \Sigma^{-1}U^T Gx &= \Sigma^{-1}U^T b, \\ V^T x &= \Sigma^{-1}U^T b. \end{aligned}$$

Setting $A = V^T$ and $y = \Sigma^{-1}U^T b$ completes the proof. \square

Lemma B.2. (Block structure of Gram matrix of anisotropically undersampled FT) Consider a d -dimensional complex-valued array x defined on a Cartesian grid of size $N = T_0 \times T_1 \times T_2 \times \dots \times T_{d-1}$. Let $\mathcal{D} = \{0, 1, 2, \dots, d-1\}$ denote the possible indices of the different underlying Cartesian axes. Further, let $\mathcal{E} \subset \mathcal{D}$ denote the indices of axes along which exhaustive samples are taken, and $\mathcal{P} = \mathcal{D} \setminus \mathcal{E}$, the remaining indices which are sampled partially. Then $\mathcal{D} = \mathcal{E} \cup \mathcal{P}$ and, with $d_{\mathcal{E}} = \#\mathcal{E}$ exhaustively sampled dimensions and $d_{\mathcal{P}} = \#\mathcal{P}$ partially sampled dimensions, $d = d_{\mathcal{E}} + d_{\mathcal{P}}$. Let the end-to-end measurement operator be represented by the $n \times N$ complex-valued matrix A . Then, the complex Hermitian Gram matrix $G = A^* A \in \mathbb{C}^{N \times N}$ is block-diagonal with $\prod_{j \in \mathcal{E}} T_j$ identical blocks each of size $\prod_{j \in \mathcal{P}} T_j$.

The corresponding result for real-valued A and real-valued symmetric $A^T A$ also holds.

Proof. Let $\mathcal{K} \subset \mathbf{R}^d$ denote the set of all tuples $k = (k_0, \dots, k_{d-1})$ that get sampled. Let e_j denote the j -th standard unit basis vector, $j = 0, \dots, d-1$, let $V_{\mathcal{E}} \subset \mathbf{R}^d$ denote the linear span of $\{e_j, j \in \mathcal{E}\}$, let $\mathcal{K}_{\mathcal{E}} = \text{Proj}_{V_{\mathcal{E}}} \mathcal{K}$ denote the orthogonal projection of the sampled tuples on the (span of the) exhaustively sampled dimensions. Correspondingly let $V_{\mathcal{P}} \subset \mathbf{R}^d$ denote the linear span of $\{e_j, j \in \mathcal{P}\}$, let $\mathcal{K}_{\mathcal{P}} = \text{Proj}_{V_{\mathcal{P}}} \mathcal{K}$ denote the projection of the sampled tuples on the (span of the) partially sampled dimensions. Then $\mathcal{K}_{\mathcal{E}}$ is, speaking informally, a Cartesian product of intervals. Formally, for each index of an exhaustively sampled dimension $j \in \mathcal{E}$, let $\mathcal{K}_j = \{0, \dots, T_j - 1\}$ denote the full range of that index. Then $\mathcal{K}_{\mathcal{E}}$ is an orthogonal sum $\mathcal{K}_{\mathcal{E}} = \bigoplus_{j \in \mathcal{E}} \mathcal{K}_j \cdot e_j$ and \mathcal{K} itself is an orthogonal sum

$$\mathcal{K} = \mathcal{K}_{\mathcal{P}} \bigoplus \mathcal{K}_{\mathcal{E}},$$

Informally, \mathcal{K} is an ‘irregular’ set of indices $\mathcal{K}_{\mathcal{P}}$ ‘times’ a Cartesian product $\mathcal{K}_{\mathcal{E}}$, and its cardinality obeys the product formula: $\#\mathcal{K} = \#\mathcal{K}_{\mathcal{P}} \times \#\mathcal{K}_{\mathcal{E}}$. A certain multiplicative relation generalizes the product formula. For each tuple $k \in \mathcal{K}$, let $k_{\mathcal{P}}$ denote the projection $\text{Proj}_{V_{\mathcal{P}}} k$ and similarly let $k_{\mathcal{E}} = \text{Proj}_{V_{\mathcal{E}}} k$. For an expression $c(k)$ obeying the factorization $c(k) = a(k_{\mathcal{E}})b(k_{\mathcal{P}})$, we have

$$\sum_{k \in \mathcal{K}} c(k) = \sum_{k \in \mathcal{K}} a(k_{\mathcal{E}})b(k_{\mathcal{P}}) = \left[\sum_{k_{\mathcal{E}} \in \mathcal{K}_{\mathcal{E}}} a(k_{\mathcal{E}}) \right] \cdot \sum_{k_{\mathcal{P}} \in \mathcal{K}_{\mathcal{P}}} b(k_{\mathcal{P}}). \quad (9)$$

The (k, t) element of the Fourier matrix can be written

$$F_k(t) = \frac{1}{\sqrt{N}} \exp \left\{ 2\pi i \left(\sum_{j=0}^{d-1} k_j t_j / T_j \right) \right\},$$

where $t = (t_0, \dots, t_{d-1})$, and $k = (k_0, \dots, k_{d-1})$. The inner product between two distinct columns u and t of A is

thus given by

$$\begin{aligned}
G_{t,u} &= (A^*A)_{t,u} = \sum_{k \in \mathcal{K}} F_k(t) F_k^*(u) \\
&= \frac{1}{N} \sum_{k \in \mathcal{K}} \exp \left(2\pi i \sum_{j \in \mathcal{D}} k_j (t_j - u_j) / T_j \right) \\
&= \frac{1}{N} \sum_{k \in \mathcal{K}} \exp \left(2\pi i \cdot \left[\sum_{j \in \mathcal{P}} k_j (t_j - u_j) / T_j + \sum_{j \in \mathcal{E}} k_j (t_j - u_j) / T_j \right] \right) \\
&= \frac{1}{\prod_{j \in \mathcal{P}} T_j} \sum_{t \in \mathcal{T}} \exp \left(2\pi i \sum_{j \in \mathcal{P}} k_j (t_j - u_j) / T_j \right) \times \left[\frac{1}{\prod_{j \in \mathcal{E}} T_j} \exp \left(2\pi i \sum_{j \in \mathcal{E}} k_j (t_j - u_j) / T_j \right) \right] \\
&= \frac{1}{\prod_{j \in \mathcal{P}} T_j} \sum_{k \in \mathcal{K}_{\mathcal{P}}} \exp \left(2\pi i \sum_{j \in \mathcal{P}} k_j (t_j - u_j) / T_j \right) \times \left[\frac{1}{\prod_{j \in \mathcal{E}} T_j} \sum_{t \in \mathcal{T}_{\mathcal{E}}} \exp \left(2\pi i \sum_{j \in \mathcal{E}} k_j (t_j - u_j) / T_j \right) \right]
\end{aligned}$$

where we used $N = \prod_{j \in \mathcal{E}} T_j \cdot \prod_{j \in \mathcal{P}} T_j$ as well as the multiplicative relation (9) for the multiplicative expression $c(k) = \exp \left(2\pi i \sum_{j \in \mathcal{D}} k_j (t_j - u_j) / T_j \right) = a(k_{\mathcal{E}}) b(k_{\mathcal{P}})$ with $a(k_{\mathcal{E}}) = \exp \left(2\pi i \sum_{j \in \mathcal{E}} k_j (t_j - u_j) / T_j \right)$ and $b(k_{\mathcal{P}}) = \exp \left(2\pi i \sum_{j \in \mathcal{P}} k_j (t_j - u_j) / T_j \right)$. Recall the Dirichlet sum formula: for an integer $u \in \{0, 1, \dots, T-1\}$,

$$\sum_{k=0}^{T-1} \exp \left(\frac{2\pi u}{T} k i \right) = \begin{cases} T & u = 0 \\ 0 & u \neq 0 \end{cases}.$$

Apply this to each exhaustively-sampled coordinate $j \in \mathcal{E}$, obtaining:

$$\frac{1}{T_j} \sum_{\mathcal{K}_j} \exp(2\pi i k_j (t_j - u_j) / T_j) = \delta(t_j - u_j), \quad j \in \mathcal{E},$$

where $\delta(\cdot)$ denotes the usual Kronecker symbol. We have

$$G_{t,u} = \frac{1}{\prod_{j \in \mathcal{P}} T_j} \sum_{k \in \mathcal{K}_{\mathcal{P}}} \exp \left(2\pi i \sum_{j \in \mathcal{P}} k_j (t_j - u_j) / T_j \right) \times \prod_{j \in \mathcal{E}} \delta(t_j - u_j). \quad (10)$$

We see that $G_{t,u} = 0$ unless $t_j = u_j$ for all $j \in \mathcal{E}$. This indeed is the advertised block structure. \square

Lemma B.3. (Singular vectors of the Gram matrix) Consider the Gram matrix $G = A^*A$ in a special case of Lemma B.2, where $d = 2$ and $\mathcal{E} = \{0\}$, $\mathcal{P} = \{1\}$, so A implements anisotropic undersampling of the 2D Fourier transform on $T_0 \times T_1$ arrays. Namely, assume that the Fourier transform is followed by selection of columns $k_{1,i}$, $0 \leq k_{1,i} < T_1$ with exhaustive sampling of all entries $\{(k_0, k_{1,i}) : 0 \leq k_0 < T_0\}$ in each selected column. Necessarily $i = 1, \dots, M \equiv n/T_0$. By Lemma B.2, G is block-diagonal with T_0 identical blocks of size $T_1 \times T_1$. Let $G^{(1)}$ represent the upper left diagonal such $T_1 \times T_1$ block. Then, $\text{rank}(G^{(1)}) = M$ and the M principal eigenvectors of the T_1 by T_1 matrix $G^{(1)}$ are given by:

$$V_\ell = (1, w_\ell, w_\ell^2, \dots, w_\ell^{T_1-1}), \quad \ell \in \mathcal{K}_1,$$

where $w_\ell = \exp(2\pi i \ell / T_1)$ and $\mathcal{K}_1 = (k_{1,i})_{i=1}^M$ denotes the collection of all sampled column indices.

Proof. We prove that for $\ell \in \mathcal{K}_1$, V_ℓ is an eigenvector by verifying $\sum_{\ell=0}^{N-1} G^{(1)}(t, u) V_\ell(u) = \lambda_\ell V_\ell(t)$, in fact by showing that $\lambda_\ell = 1$. Lemma B.2 – specifically (10) – gives us that for $k = (k_0, k_1)$ and

$$G_{t,u} = \left(\frac{1}{\prod_{j \in \mathcal{P}} T_j} \sum_{k \in \mathcal{K}_{\mathcal{P}}} \exp \left(2\pi i \cdot \sum_{j \in \mathcal{P}} k_j (t_j - u_j) / T_j \right) \right) \cdot \prod_{j \in \mathcal{E}} \delta(t_j - u_j).$$

Because $d = 2$ and k_0 is sampled exhaustively, the upper left $T_1 \times T_1$ block has the form:

$$G_{(0,t),(0,u)} = \frac{1}{T_1} \sum_{k \in \mathcal{K}_1} \exp(2\pi i k(t-u)/T_1), \quad (t, u) \in \{0, \dots, T_1 - 1\}^2,$$

where now k, t , and u are integers. The matrix $G^{(1)}$ has entries $G^{(1)}(t, u) \equiv G_{(0,t),(0,u)}$ for $0 \leq t, u < T_1$. It has rank $M = \#\mathcal{T}_1$ by inspection of the preceding display.

$$\begin{aligned} \sum_{u=0}^{T_1-1} G^{(1)}(t, u) V_\ell(u) &= \sum_{u=0}^{T_1-1} \left(\frac{1}{T_1} \sum_{k \in \mathcal{K}_1} \exp(2\pi i k(t-u)/T_1) \right) \exp(2\pi i u \ell / T_1) \\ &= \sum_{k \in \mathcal{K}_1} \left(\frac{1}{T_1} \exp(2\pi i k t / T_1) \right) \left(\sum_{u=0}^{T_1-1} \exp(2\pi i u(k-\ell)/T_1) \right) \\ &= \sum_{k \in \mathcal{K}_1} \left(\frac{1}{T_1} \exp(2\pi i k t / T_1) \right) (T_1 \delta(k-\ell)) \\ &= \exp(2\pi i \ell t / T_1) = V_\ell(t). \end{aligned}$$

□

Proof of Theorem 5.2. Consider the two convex optimization problems

$$(P_1) \quad \min \|x\|_{1, \mathbb{C}^N} \quad \text{subject to} \quad Ax = y,$$

$$(P_2) \quad \min \|x\|_{1, \mathbb{C}^N} \quad \text{subject to} \quad A^*Ax = A^*y,$$

where A is an $n \times N$ ($n < N$) matrix having n nonzero singular values (i.e., A has full row rank). Problem (P_1) is equivalent to (P_2) because A^* has full column rank n ; hence their solution sets match. By Lemma B.2, $G = A^*A$ is block-diagonal. By separability of ℓ_1 minimization, we can solve the T_0 block subproblems each of size $T_1 \times T_1$ individually. Because blocks are identical and $\text{rank}(G) = \lfloor \delta T_1 \rfloor T_2$, $\text{rank}(G^b) = \lfloor \delta T_1 \rfloor$ for blocks $b = 1, \dots, N$. By Lemma B.1, we know that we can solve equivalent full-row-rank problems of size $\lfloor \delta T_1 \rfloor \times T_2$ as long as we find the right singular vectors. By Lemma B.3 we know that right singular vectors are defined by the partial Fourier matrix. □

C Proof of Theorem 9.1

The arguments of Appendix B can all be redone, step-by-step, replacing the field \mathbb{C} by the hypercomplex algebra \mathbf{H}_d . The notation and basic pattern of argument are given in [36] and we won't repeat them. The basic idea is as follows. Let $n' = n/2^d$ and $N' = N/2^d$. The matrix A belongs to $\mathbf{H}_d^{n' \times N'}$, the matrix $G = A^\#A$ belongs to $\mathbf{H}_d^{N' \times N'}$ (here $\#$ denotes hypercomplex conjugation; again, see [36] for details). The hypercomplex entries $x(i)$ can be viewed as 2^d dimensional real vectors. The ℓ_1 norm can then be written:

$$\|x\|_{1, \mathbf{H}_d} = \sum_{i=1}^{N'} \|x(i)\|_{\ell_1^{2^d}(\mathbf{R})}.$$

The arguments of the preceding section go through without essential changes; the Dirichlet sum has this direct analog:

$$\sum_{t=0}^{T-1} \exp_{\mathbf{H}_d} \left(\frac{2\pi t}{T} u \mathbf{i} \right) = \begin{cases} T & u = 0 \\ 0 & u \neq 0 \end{cases},$$

where $u \in \{0, \dots, T-1\}$, and $\exp_{\mathbf{H}_d}$ denotes the exponential function defined by the usual power series within the associative algebra \mathbf{H}_d .

References

- [1] Mosek optimization software. Available online via <http://www.mosek.com>.
- [2] D. Amelunxen, M. Lotz, M. B. McCoy, and J. A. Tropp. Living on the edge: Phase transitions in convex programs with random data. *Information and Inference*, 3:224–294, 2014.
- [3] L. Applebaum, S. Howard, S. Searle, and R. Calderbank. Chirp sensing codes: Deterministic compressed sensing measurements for fast recovery. *Applied and Computational Harmonic Analysis*, 26(2):283–290, 2009.
- [4] E. J. Candès and T. Tao. Decoding by linear programming. *IEEE Trans. on Inform. Theory*, 51:4203–4215, 2005.
- [5] D. L. Donoho. Neighborly polytopes and sparse solution of underdetermined linear equations. *Technical Report, Department of Statistics, Stanford University*, 2004.
- [6] D. L. Donoho. Compressed sensing. *IEEE Transactions on Information Theory*, 52:489–509, April 2006.
- [7] D. L. Donoho and Xiaoming Huo. Uncertainty principles and ideal atomic decomposition. *IEEE Trans. Inform. Theory*, 47(7):2845–2862, 2001.
- [8] D. L. Donoho, I. Johnstone, and A. Montanari. Accurate prediction of phase transitions in compressed sensing via a connection to minimax denoising. *IEEE Transactions on Information Theory*, 59(6):3396–3433, June 2013.
- [9] D. L. Donoho, A. Maleki, and A. Montanari. Message passing algorithms for compressed sensing. *PNAS*, 106:18914–18919, 2009.
- [10] D. L. Donoho and J. Tanner. Neighborliness of randomly-projected simplices in high dimensions. *PNAS*, 102(27):9452–9457, 2005.
- [11] D. L. Donoho and J. Tanner. Counting faces of randomly projected polytopes when the projection radically lowers dimension. *Journal of American Mathematical Society*, 22:1–53, 2009.
- [12] D. L. Donoho and J. Tanner. Counting faces of randomly-projected polytopes when the projection radically lowers dimension. *J. AMS*, 22:1–53, 2009.
- [13] D. L. Donoho and J. Tanner. Observed universality of phase transitions in high-dimensional geometry, with implications for modern data analysis and signal processing. *Phil. Trans. R. Soc.*, 367:4273–4293, 2009.
- [14] D. L. Donoho and J. Tanner. Counting the faces of randomly-projected hypercubes and orthants, with applications. *Discrete & Computational Geometry*, 43(3):522–541, 2010.
- [15] D. L. Donoho and J. Tanner. Exponential bounds implying construction of compressed sensing matrices, error-correcting codes and neighborly polytopes by random sampling. *IEEE Transactions on Information Theory*, 56(4), 2010.
- [16] Armin Eftekhari, Han Lun Yap, Christopher J. Rozell, and Michael B. Wakin. The restricted isometry property for random block diagonal matrices. *Applied and Computational Harmonic Analysis*, 38(1):1 – 31, 2015.
- [17] L. Feng, T. Benkert, K. T. Block, D. K. Sodickson, R. Otazo, and H. Chandarana. Compressed sensing for body MRI. *Journal of Magnetic Resonance Imaging*, 2016.
- [18] J. E. Fowler, S. Mun, and E. W. Tramel. Block-based compressed sensing of images and video. *Foundations and Trends in Signal Processing*, 4(4):297–416, 2012.
- [19] S. Friedland, Q. Li, and D. Schonfeld. Compressive sensing of sparse tensors. *IEEE Trans. Image Process.*, 23(10), October 2014.
- [20] M. Friedlander and M. Saunders. ASP: A set of Matlab functions for solving Basis Pursuit-type problems., 2010. Available online via <http://web.stanford.edu/group/SOL/software/asp/>.

- [21] M. Friedlander and M. Saunders. A dual active-set quadratic programming method for finding sparse least-squares solutions. *DRAFT Technical Report, Department of Computer Science, University of British Columbia*, July 30 2012. Available online via <http://web.stanford.edu/group/SOL/software/asp/bpdual.pdf>.
- [22] M. Grant and S. Boyd. CVX: Matlab software for disciplined convex programming, version 1.21, May 2010. Available online via <http://cvxr.com/cvx>.
- [23] A. Greiser and M. von Kienlin. Efficient k-space sampling by density-weighted phase-encoding. *Magnetic resonance in Medicine*, 50(6):1266–1275, 2003.
- [24] J. C. Hoch, M. W. Maciejewski, M. Mobli, A. D. Schuyler, and A. S. Stern. Nonuniform sampling and maximum entropy reconstruction in multidimensional NMR. *Accounts of chemical research*, 47(2):708–717, 2014.
- [25] S.D. Howard, A.R. Calderbank, and S.J. Searle. A fast reconstruction algorithm for deterministic compressive sensing using second order reed-muller codes. In *Information Sciences and Systems, 2008. CISS 2008. 42nd Annual Conference on*, IEEE Conference on Information, Science and Systems, pages 11–15. IEEE, March 2008.
- [26] Q. Li, D. Schonfeld, and S. Friedland. Generalized tensor compressive sensing. *IEEE International Conference on Multimedia & Expo*, 2013.
- [27] G. Lu. Block compressed sensing of natural images. *15th IEEE International Conference on Digital Signal Processing*, pages 403–406, 2007.
- [28] M. Lustig, D. L. Donoho, and J. M. Pauly. Sparse MRI: The application of compressed sensing for rapid MR imaging. *Magnetic Resonance in Medicine*, 58(6):1182–1195, 2007.
- [29] M. Lustig, D. L. Donoho, J. M. Santos, and J. M. Pauly. Compressed sensing MRI. *IEEE Signal Processing Magazine*, 72, 2008.
- [30] B. Madore, G. H. Glover, N. J. Pelc, et al. Unaliasing by fourier-encoding the overlaps using the temporal dimension (UNFOLD), applied to cardiac imaging and fMRI. *Magnetic Resonance in Medicine*, 42(5):813–828, 1999.
- [31] G. J. Marseille, R. De Beer, M. Fuderer, A. F. Mehlkopf, and D. Van Ormondt. Nonuniform phase-encode distributions for MRI scan time reduction. *Journal of Magnetic Resonance*, 111(1):70–75, 1996.
- [32] G. McGibney, M. R. Smith, S. T. Nichols, and A. Crawley. Quantitative evaluation of several partial Fourier reconstruction algorithms used in MRI. *Magnetic Resonance in Medicine*, 30(1):51–59, 1993.
- [33] M. Mobli, M. W. Maciejewski, A. D. Schuyler, A. S. Stern, and J. C. Hoch. Sparse sampling methods in multidimensional NMR. *Physical Chemistry Chemical Physics*, 14(31):10835–10843, 2012.
- [34] H. Monajemi and D. L. Donoho. Clusterjob, a automated system for reproducibility and hassle-free submission of computational jobs to clusters. 2015. Available online via <https://github.com/monajemi/clusterjob>.
- [35] H. Monajemi and D. L. Donoho. Code and data supplement to "Sparsity/undersampling tradeoffs in anisotropic undersampling, with applications in MR imaging/spectroscopy". *Stanford Digital Repository*, 2017. Available online via <https://purl.stanford.edu/th702qm4100>.
- [36] H. Monajemi, D. L. Donoho, J. C. Hoch, and A. D. Schuyler. Incoherence of partial-component sampling in multidimensional NMR. *arXiv:1702.01830*, 2017.
- [37] H. Monajemi, S. Jafarpour, M. Gavish, Stat 330/CME 362 Collaboration, and D. L. Donoho. Deterministic matrices matching the compressed sensing phase transitions of Gaussian random matrices. *PNAS*, 110(4):1181–1186, 2013.

- [38] S. Oymak and J. A. Tropp. Universality laws for randomized dimension reduction, with applications. *arXiv:1511.09433*, 2015.
- [39] K. P. Pruessmann, M. Weiger, M. B. Scheidegger, P. Boesiger, et al. SENSE: sensitivity encoding for fast MRI. *Magnetic Resonance in Medicine*, 42(5):952–962, 1999.
- [40] P. Schmieder, A. S. Stern, G. Wagner, and J. C. Hoch. Application of nonlinear sampling schemes to COSY-type spectra. *Journal of Biomolecular NMR*, 3(5):569–576, 1993.
- [41] P. Schmieder, A. S. Stern, G. Wagner, and J. C. Hoch. Improved resolution in triple-resonance spectra by nonlinear sampling in the constant-time domain. *Journal of Biomolecular NMR*, 4(4):483–490, 1994.
- [42] D. K. Sodickson and W. J. Manning. Simultaneous acquisition of spatial harmonics (SMASH): fast imaging with radiofrequency coil arrays. *Magnetic Resonance in Medicine*, 38(4):591–603, 1997.
- [43] J. I. Tamir, M. Uecker, W. Chen, P. Lai, M. T. Alley, S. S. Vasanawala, and M. Lustig. T2 shuffling: Sharp, multicontrast, volumetric fast spin-echo imaging. *Magnetic Resonance in Medicine*, 2016.
- [44] T. Tao. An uncertainty principle for cyclic groups of prime order. *Mathematical Research Letters*, 2(1), 2005.
- [45] J. A. Tropp and A. C. Gilbert. Signal recovery from random measurements via orthogonal matching pursuit. *IEEE Trans. Inform. Theory*, 53(12):4655–4666, 2007.
- [46] S. S. Vasanawala, M. T. Alley, B. A. Hargreaves, R. A. Barth, J. M. Pauly, and M. Lustig. Improved pediatric MR imaging with compressed sensing. *Radiology*, 256(2):607–616, 2010.
- [47] T. Zhang, U. Yousaf, A. Hsiao, J. Y. Cheng, M. T. Alley, M. Lustig, J. M. Pauly, and S. S. Vasanawala. Clinical performance of a free-breathing spatiotemporally accelerated 3-D time-resolved contrast-enhanced pediatric abdominal MR angiography. *Pediatric Radiology*, 45(11):1635–1643, 2015.
- [48] B. Zhao, J. P. Haldar, A. G. Christodoulou, and Z. Liang. Image reconstruction from highly undersampled (k, t) -space data with joint partial separability and sparsity constraints. *IEEE Transactions on Medical Imaging*, 31(9):1809–1820, 2012.